NUREG/CR--4744-Vol.3-No.1

TI90 007411

Long-Term Embrittlement of Cast Duplex Stainless Steels in LWR Systems

Semiannual Report
October 1987–March 1988

Manuscript Completed: April 1989
Date Published: February 1990

Prepared by
O. K. Chopra, H. M. Chung

Argonne National Laboratory
9700 South Cass Avenue
Argonne, IL 60439

Prepared for
Division of Engineering
Office of Nuclear Regulatory Research
U.S. Nuclear Regulatory Commission
Washington, DC 20555
NRC FIN A2243

Previous Documents in Series

Long-Term Embrittlement of Cast Duplex Stainless Steels in LWR Systems: Annual Report October 1982–September 1983, NUREG/CR–3857, ANL–84–44 (August 1984).

Long-Term Embrittlement of Cast Duplex Stainless Steels in LWR Systems: Annual Report October 1983–September 1984, NUREG/CR-4204, ANL-85-20 (March 1985).

Long-Term Embrittlement of Cast Duplex Stainless Steels in LWR Systems: Annual Report October 1984–September 1985, NUREG/CR-4503, ANL-86-3 (January 1986).

Long-Term Embrittlement of Cast Duplex Stainless Steels in LWR Systems: Semiannual Report October 1985–March 1986, NUREG/CR-4744 Vol. I, No. 1, ANL-86-54 (September 1986).

Long-Term Embrittlement of Cast Duplex Stainless Steels in LWR Systems: Semiannual Report April–September 1986, NUREG/CR-4744 Vol. I, No. 2, ANL-87-16 (March 1987).

Long-Term Embrittlement of Cast Duplex Stainless Steels in LWR Systems: Semiannual Report October 1986–March 1987, NUREG/CR-4744, Vol. 2, No. 1, ANL-87-45 (July 1987).

Long-Term Embrittlement of Cast Duplex Stainless Steels in LWR Systems: Semiannual Report April-September 1987, NUREG/CR-4744, Vol. 2, No. 2, ANL-89/6 (July 1989).

Long–Term Embrittlement of Cast Duplex Stainless Steels in LWR Systems

by

O. K. Chopra and H. M. Chung

Abstract

This progress report summarizes work performed by Argonne National Laboratory on long-term embrittlement of cast duplex stainless steels in LWR systems during the six months from October 1987 to March 1988. A mechanistic understanding of the activation energy of aging is described on the basis of the results of microstructural characterization of various heats of Grades CF–3, CF–8, and CF–8M stainless steel that were used in aging studies at different laboratories. The kinetics of the spinodal decomposition of ferrite (i.e., the primary mechanism of aging embrittlement) appear to be strongly influenced by a synergistic effect of G–phase nucleation and growth. When the activation energies (ranging from 18 to 50 kcal/mole) were plotted as a function of the volume fraction of G phase produced during accelerated aging, a good correlation was obtained regardless of variations in grade, bulk chemical composition, and fabrication process. Spinodal–like decomposition of austenite in heats containing a relatively high level of Ni has also been investigated. Charpy-impact data for thermally aged cast stainless steel were analyzed to determine the kinetics and extent of embrittlement. The ferrite morphology had a strong effect on the extent of embrittlement, whereas the material composition influenced the kinetics of embrittlement. Results obtained from the present study of mechanical properties, and data of other investigators were analyzed to develop the procedure and correlations for predicting the kinetics and extent of embrittlement, under reactor operating conditions, from the material parameters.

Contents

List of Figures

List of Tables

Executive Summary

A program is being conducted to investigate the significance of in-service embrittlement of cast duplex stainless steels under light-water reactor operating conditions. Microstructures of cast materials subjected to long-term aging in either the laboratory or reactor service have been characterized by various analytical techniques. The results indicate that the aging embrittlement is caused primarily by spinodal decomposition of the ferrite phase. Carbide formation on ferrite/austenite boundaries is an additional but secondary process of embrittlement for high-carbon materials. The spinodal decomposition is accompanied by a simultaneous nucleation and growth of G phase, resulting in complex synergistic effects on the aging kinetics. We have obtained microstructure-based mechanistic correlation that can be used to effectively predict the activation energy of aging, which can be used to extrapolate laboratory data to reactor operating conditions.

Charpy-impact data for thermally aged cast stainless steel were analyzed to determine the kinetics and extent of embrittlement. The material composition and the ferrite content and spacing are important parameters in controlling embrittlement of cast stainless steels. The extent of embrittlement depends on ferrite morphology, whereas the kinetics of embrittlement can vary significantly with the composition of the cast material since the activation energy for embrittlement is in the range of 90 to 235 kJ/mole (20 to 56 kcal/mole). Results obtained from the present study of mechanical properties, and data from other investigations were analyzed to develop the procedure and correlations for predicting the kinetics and extent of embrittlement, under reactor operating conditions, from the material parameters.

The loss of toughness of cast stainless steels due to low-temperature embrittlement can be recovered by a short-term anneal of 1 h at 550°C and water quenching. However, preliminary data show that the recovery annealed material reembrittles in a relatively short time.

1 Introduction

Cast duplex stainless steels are used extensively in the nuclear industry for valve bodies, pump casings, and primary coolant piping. The ferrite phase in the duplex structure of austenitic-ferritic stainless steels increases the tensile strength and improves the soundness of casting, weldability, and resistance to stress corrosion cracking of these steels. However, various carbide phases, intermetallic compounds such as sigma and chi phases, and the chromium-rich bcc phase (α') can precipitate in the ferrite phase during service at elevated temperatures and lead to substantial degradation of mechanical properties. It has long been known that ferritic stainless steels are susceptible to severe embrittlement when exposed to temperatures in the range of 300 to 500°C, owing to the precipitation of the α' phase.[1-3] The potential for significant embrittlement of cast duplex stainless steels has been confirmed by recent studies on cast materials that were aged at temperatures between 300 and 450°C for times up to 70,000 h (~8 yr).[4-9] Room temperature impact strength can be reduced by ~80% after aging for ~8 yr at temperatures as low as 300°C. An increase in the ferrite content of the cast structure increases the susceptibility to embrittlement.

The primary objectives of this program are to (1) investigate the significance of in-service embrittlement of cast duplex stainless steels under light-water-reactor (LWR) operating conditions, and (2) evaluate possible remedies for the embrittlement problem in existing and future plants. The scope of the program includes the following goals: (1) characterize and correlate the microstructure of in-service reactor components and laboratory-aged material with loss of fracture toughness to establish the mechanism of aging and to validate the simulation of in-reactor degradation by accelerated aging, (2) establish the effects of key compositional and metallurgical variables on the kinetics and extent of embrittlement, and (3) obtain fracture toughness data on long-term-aged materials to predict the degree of toughness loss suffered by cast stainless steel components during normal and extended service life of reactors.

Microstructural and mechanical-properties data are being obtained on 19 experimental heats (static-cast keel blocks) and six commercial heats (centrifugally cast pipes and a static-cast pump impeller and pump casing ring) as well as reactor-aged material of grades CF-3, CF-8, and CF-8M cast stainless steels. Six of the experimental heats are also in the form of 76-mm-thick slabs. Specimen blanks for Charpy-impact, tensile, and J-R curve tests are being aged at 290, 320, 350, 400, and 450°C for times up to 50,000 h. The reactor-aged material is from the recirculating-pump cover plate assembly of the KRB reactor, which was in service in Gundremmingen, West Germany for ~12 yr (~8 yr at a service temperature of 284°C). Fractured impact test bars from five heats of aged cast stainless steel were obtained from the Georg Fischer Co. (GF), Switzerland, for microstructural characterization. The materials are from a previous study of long-term aging behavior of cast stainless steel.[4] The data on chemical composition, ferrite content, hardness, ferrite morphology, and grain structure of the experimental and commercial heats have been reported earlier.[10-14] The chemical composition, hardness, and ferrite content and distribution of some of the cast materials are given in Table 1. The results of microstructural characterization and mechanical-property data from Charpy-impact, tensile, and J-R curve tests on 16 heats of cast stainless steel aged up to 10,000 h at temperatures between 290 and 450°C have also been presented earlier.[15-19]

Table 1. Product Form, Chemical Analysis, Hardness, and Ferrite Morphology of Various Heats of Cast Stainless Steel

Heat	Grade	Product Form	Size (mm)	Composition (wt.%)							Hardness	Ferrite Content (%)		Ferrite Intercept
				C	N	Mn	Si	Ni	Cr	Mo	R_B	Calc.	Meas.	(μm)
56	CF-8	Keel B.	180 x 120 x 30-90	0.066	0.030	0.57	1.05	9.28	19.65	0.34	82.5	7.3	10.1	84
59	CF-8			0.062	0.045	0.60	1.08	9.34.	20.33	0.32	83.2	8.8	13.5	75
61	CF-8			0.054	0.080	0.65	1.01	8.86	20.65	0.32	85.2	10.0	13.1	82
60	CF-8			0.064	0.058	0.67	0.95	8.34	21.05	0.31	86.7	15.1	21.1	63
47	CF-3			0.018	0.028	0.60	1.06	10.63	19.81	0.59	79.6	8.4	16.3	68
52	CF-3			0.009	0.052	0.57	0.92	9.40	19.49	0.35	81.6	10.3	13.5	69
51	CF-3			0.010	0.058	0.63	0.86	9.06	20.13	0.32	83.8	14.2	18.0	52
63	CF-8M			0.055	0.031	0.61	0.58	11.85	19.37	2.57	81.5	6.4	10.4	81
65	CF-8M			0.049	0.064	0.50	0.48	9.63	20.78	2.57	89.9	20.9	23.4	43
64	CF-8M			0.038	0.038	0.60	0.63	9.40	20.76	2.46	89.7	28.9	28.4	41
P1	CF-8	Pipe	890 OD 63 wall	0.036	0.056	0.59	1.12	8.10	20.49	0.04	84.9	17.7	24.1	90
P2	CF-3	Pipe	930 OD 73 wall	0.019	0.040	0.74	0.94	9.38	20.20	0.16	83.8	12.4	15.6	69
I	CF-3	Impeller	NA	0.019	0.032	0.47	0.83	8.65	20.14	0.45	81.0	20.9	17.1	65
P4	CF-8M	Pipe	580 OD 32 wall	0.040	0.151	1.07	1.02	10.00	19.64	2.05	83.1	5.9	10.4	182
68	CF-8	Slab	610 x 610 x 76	0.063	0.062	0.64	1.07	8.08	20.64	0.31	84.6	14.9	23.4	87
69	CF-3	Slab	610 x 610 x 76	0.023	0.028	0.63	1.13	8.59	20.18	0.34	83.7	21.0	23.6	35
74	CF-8M	Slab	610 x 610 x 76	0.064	0.048	0.54	0.73	9.03	19.11	2.51	85.8	15.5	18.4	90
75	CF-8M	Slab	610 x 610 x 76	0.065	0.052	0.53	0.67	9.12	20.86	2.58	89.5	24.8	27.8	73
KRB	CF-8	Pump Cover Plate		0.062	0.038	0.31	1.17	8.03	21.99	0.17	-	27.7	34.0	173

The experimental effort during the past six months has focused on (1) characterization of the microstructure of reactor-aged and long-term laboratory-aged material and (2) mechanical properties of medium-term laboratory-aged material.

2 Aging Kinetics and Microstructural Characteristics (H. M. Chung)

2.1 Introduction

In a number of previous reports,[15-20] several metallurgical processes have been identified in association with thermal aging embrittlement of CF-3, CF-8, and CF-8M cast stainless steels in the temperature range of 280–400°C. Five processes have been identified in the ferrite phase,[16,18] two in austenite,[16,20] and two at the ferrite–austenite boundaries.[16-18] The primary mechanism of aging embrittlement in these processes is spinodal decomposition of ferrite, which involves Fe, Cr, and Ni segregation on a very fine scale of several atomic distances. For high-C CF-8 or CF-8A (but not the Mo-containing CF-8M) materials, $M_{23}C_6$ carbide precipitation on the ferrite–austenitic boundaries is the secondary embrittlement mechanism.

However, the spinodal decomposition is accompanied by a simultaneous precipitation of the Si- and Ni-rich G phase, which appears to influence the aging kinetics in a synergistic manner.[16,18] The G-phase precipitation, under otherwise identical conditions, is faster at 400°C than 300°C. Thus, the synergistic effect of the G-phase nucleation and precipitation appears to be pronounced for accelerated aging at 400°C but not at 300°C. Consequently, it has been proposed that the activation energy of embrittlement (i.e., the relative kinetics of embrittlement during aging at 400 and 300°C) will be strongly influenced by the G-phase (or Ni–Si clustering) behavior at 400°C.[16] It has also been proposed that significant precipitation of the boundary $M_{23}C_6$ will influence the activation energy.[16] Since a reliable activation energy value is crucial for an assessment of long-term aging behavior at reactor operating conditions, a mechanistic correlation between the microstructural characteristics and the activation energy has been formulated during this reporting period to provide insight into the development of a better methodology of predicting the component life.

The precipitation characteristics of the G phase have been quantitatively determined by dark-field transmission electron microscopy (TEM) imaging, and the volume fraction of G phase for the various heats has been measured. For all the heats, G-phase precipitation during aging at 300°C was minimal or absent. For all the high-activation-energy heats, G-phase precipitation after aging at 400°C (for up to 30,000 h) either did not occur or occurred to a minimal extent by heterogeneous precipitation on dislocations. In contrast, all the low-activation-energy heats were characterized by copious amounts of G-phase precipitation at 400°C. When the activation energies (ranging from 18 to 50 kcal/mole) were plotted as a function of the volume fraction of G phase produced during accelerated aging, a good correlation was obtained regardless of variations in grade, bulk chemical composition, and fabrication process. This observation suggests that significant precipitation of G phase appears to slow the kinetics of spinodal decomposition; i.e., precipitation of the Ni-rich G phase, or Ni–Si clustering prior to the precipitation, will deplete the ferrite matrix of Ni. As a consequence, the spinodal decomposition will be slower than in materials and under aging conditions in which G-phase precipitation is negligible. This effect on spinodal decomposition will be significant during aging at 400°C but negligible at 300°C.

The role of Ni in the kinetics of spinodal decomposition, inferred from the correlation between the microstructure and activation energy, appears consistent with the results of field ion atom probe (FIAP) analysis conducted on Shippingport reactor valve materials. The comparison is described elsewhere in this report.

In a previous report, a preliminary observation indicated a spinodal-like decomposition of austenite in some high-Ni CF-8M heats after long-term (30,000 h) aging at 400 and 350°C.[16] Although the spinodal-like decomposition appears to be an order of magnitude slower than the spinodal decomposition of ferrite, its contribution to the overall aging process near end-of-life must be better understood, since austenite is the primary phase of the duplex cast stainless steel. Therefore, further study during this reporting period focused on the spinodal-like decomposition.

2.2 Technical Progress

2.2.1 Correlation between Microstructure and Activation Energy

A Mechanistic Model

When significant precipitation of G phase (or Ni-Si clustering prior to the G-phase precipitation) and of $M_{23}C_6$ on ferrite-austenitic boundaries occurs, aging at 400°C will be influenced more profoundly than at 300°C. Thus, the activation energy is expected to be altered, as illustrated schematically in Fig. 1. In the figure, comparative activation energies for three hypothetical cases of microstructural transformation are shown schematically, i.e., (A) spinodal decomposition only, (B) Ni-Si (or Ni-Si-Mo) clustering or G-phase nucleation and precipitation plus (A), and (C) significant $M_{23}C_6$ precipitation on the ferrite/austenite boundary during aging plus (B). Under otherwise similar conditions, Case (B) is likely to occur for heats containing relatively high levels of Si, Ni, and Mo in the ferrite. Case (C) is likely to occur for CF-8 or CF-8A heats containing a high level of C, but not for CF-8M. According to this model, the activation energy is expected to be a function of the chemical compositions that influence the G-phase and $M_{23}C_6$ precipitations.

Since the spinodal decomposition occurs on a fine scale of several atomic distances, it is likely that the early-stage Ni-Si (or Ni-Si-Mo) clustering and G-phase nucleation will influence the kinetics of the decomposition, particularly for aging at 400°C. In fact, aging embrittlement at 400°C occurs during a relatively early period, when the G-phase precipitates or nuclei are too small to be resolved by TEM. However, a later stage of G-phase precipitation and Ostwald ripening[21] is expected to be a fair indication of the relative extent of the early-stage reactions. Therefore, G-phase volume fraction, determined for different heats after aging at the same temperature (e.g., 400°C) for the same time (e.g., 10,000 or 30,000 h), will provide an indication of the relative extent of the early-stage spinodal decomposition.

Correlation with G-phase and $M_{23}C_6$ Precipitation

For long-term aging at 400°C, G-phase volume fraction can be measured by dark-field TEM imaging. A number of heats were selected for the dark-field imaging analysis. The chemical composition and ferrite content of the heats are given in Table 2. G-phase reflections could be identified readily for specimens in which the G-phase volume fraction

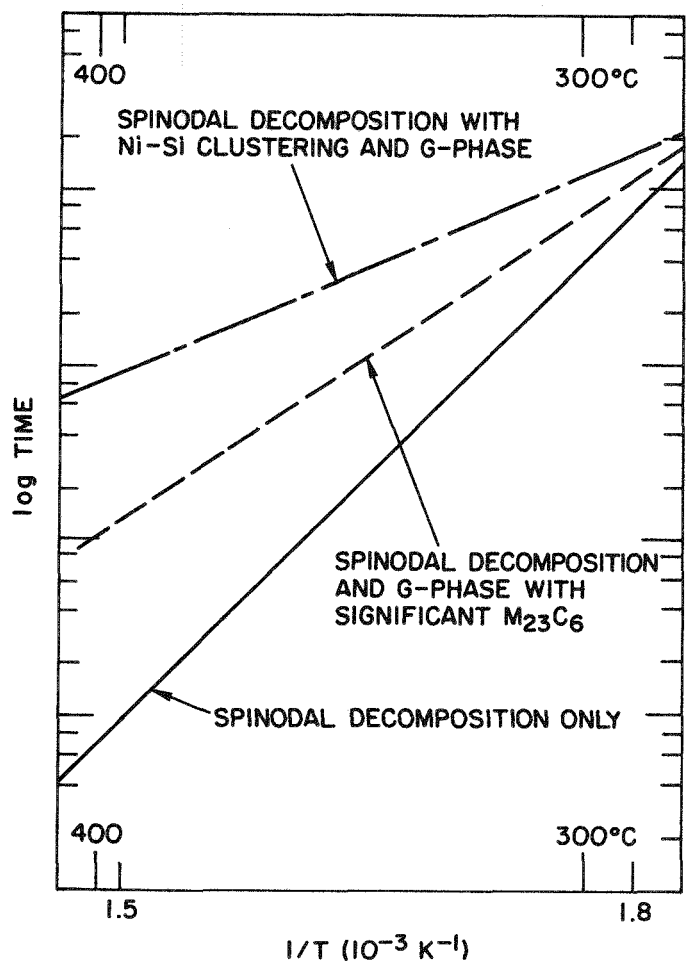

Fig. 1.

Schematic Illustration of Relative Kinetics and Activation Energies for Three Hypothetical Cases of Metallurgical Transformation under Otherwise Identical Conditions.

is high, e.g., Heats P4 and 286 aged at 400°C for >10,000 h. For specimens with smaller volume fractions, the strong {333} reflections[21] of the G phase could be identified by tilting the specimen orientation close to the (110), (311), or (133) zone of the ferrite. In many cases, even the intensity of the {333} reflections was too weak to be visible on the selected-area diffraction pattern. In such cases, the objective aperture was placed on a blind spot where the {333} reflection should be located. A dark-field image was then produced from the blind spot (e.g., Heats 60 and 51 aged at 400°C for 10,000 h). In other cases, imaging produced from a spot containing both the ferrite and G-phase reflections showed satisfactory results (e.g., Heats 59 and 292, aged at 400°C for 10,000 h).

In Fig. 2, results of TEM analysis of the G-phase size and distribution are given for eight different heats aged at 400°C for 30,000 h and one heat aged at 400°C for 70,000 h. For each heat, the activation energy determined from room temperature impact tests is given. Examination of Fig. 2 reveals a monotonic correlation between the G-phase volume fraction and the activation energy, i.e., the higher the volume fraction, the lower the energy. For high-C CF-8 Heats 56, 59, and 60, approximately 60% of the ferrite-austenite boundary was associated with $M_{23}C_6$ precipitates (Heat 56 in Fig. 2, and Heats 59 and 60 in Fig. 3). G-phase volume fraction was determined from Fig. 2, and the results were plotted against the activation energy in Fig. 4 for f_c ~0.0 and f_c ~0.6, where f_c is the fraction of the ferrite-austenite boundary covered by $M_{23}C_6$. Also included in the figure are similar data obtained for a number of heats that were tested by GE[22] and CEGB[23] and whose microstructural

Table 2. Chemical Compositions of Laboratory-Aged Heats of CF-3, CF-8, and CF-8M Duplex Stainless Steels for Microstructural Characterization and Studies of Aging Kinetics and Mechanisms

Heat No.	Grade	Composition (wt.%)									Ferrite Content (%)
		Mn	Si	Mo	Cr	Ni	P	S	N	C	
280N	CF-8	0.50	1.37	0.25	21.60	8.00	0.015	0.006	0.029	0.028	38.0
280	CF-8	0.50	1.37	0.25	21.60	8.00	0.015	0.006	0.029	0.028	38.0
278	CF-8	0.28	1.00	0.13	20.20	8.27	0.008	0.019	0.027	0.038	15.0
292	CF-8	0.34	1.57	0.13	21.60	7.52	0.018	0.016	–	0.090	28.0
286	CF-8M	0.40	1.33	2.44	20.20	9.13	0.044	0.015	0.063	0.072	22.0
47	CF-3	0.60	1.06	0.59	19.81	10.63	–	–	0.028	0.018	16.3
52	CF-3	0.57	0.92	0.35	19.49	9.40	–	–	0.052	0.009	13.5
51	CF-3	0.63	0.86	0.32	20.13	9.06	–	–	0.058	0.010	18.0
60	CF-8	0.67	0.95	0.31	21.05	8.34	–	–	0.058	0.064	21.1
56	CF-8	0.57	1.05	0.34	19.65	9.28	–	–	0.030	0.066	10.1
63	CF-8M	0.61	0.58	2.57	19.37	11.85	–	–	0.031	0.055	10.4
P4	CF-8M	1.07	1.02	2.05	19.64	10.00	–	–	0.151	0.040	10.4
64	CF-8M	0.60	0.63	2.46	20.76	9.40	–	–	0.038	0.038	28.4
65	CF-8M	0.50	0.48	2.57	20.78	9.63	–	–	0.064	0.049	23.4
74	CF-8M	0.54	0.73	2.51	19.11	9.03	–	–	0.048	0.064	18.4
75	CF-8M	0.53	0.67	2.58	20.86	9.12	–	–	0.052	0.065	27.8

characterization was reported. The results of the dark-field TEM characterization of G-phase size, density, and volume fraction are listed in Table 3 for aging at 400°C for 30,000 h. For aging at 400°C for 10,000 h, the microstructural characteristics similar to those shown in Fig. 2 and a correlation similar to that in Fig. 4 are shown in Figs. 5 and 6, respectively.

The correlations in Figs. 4 and 6 indicate that the mechanistic model of activation energy, illustrated schematically in Fig. 1, is essentially valid. For heats containing an insignificant amount of boundary $M_{23}C_6$, a high activation energy was associated with a negligible amount of G-phase precipitate (e.g., Heat 51), and, in contrast, a low activation energy was associated with a significant amount of G phase (e.g., Heat P4). This is illustrated in Fig. 7 in the form of Arrhenius plots of aging kinetics for Heats 51 and P4. When both G-phase and boundary $M_{23}C_6$ precipitation is significant (e.g., Heat 59), Arrhenius plots such as those in Fig. 8 can be expected for actual and hypothetical microstructures. In general, CF-8M materials containing Mo and a relatively high level of Ni showed more extensive G-phase precipitation but a smaller amount of the boundary $M_{23}C_6$. Thus, the activation energy of a CF-8M heat tends to be low. However, the characteristics of G-phase precipitation were complex and, in general, it was difficult to predict the behavior solely on the basis of bulk chemical composition.

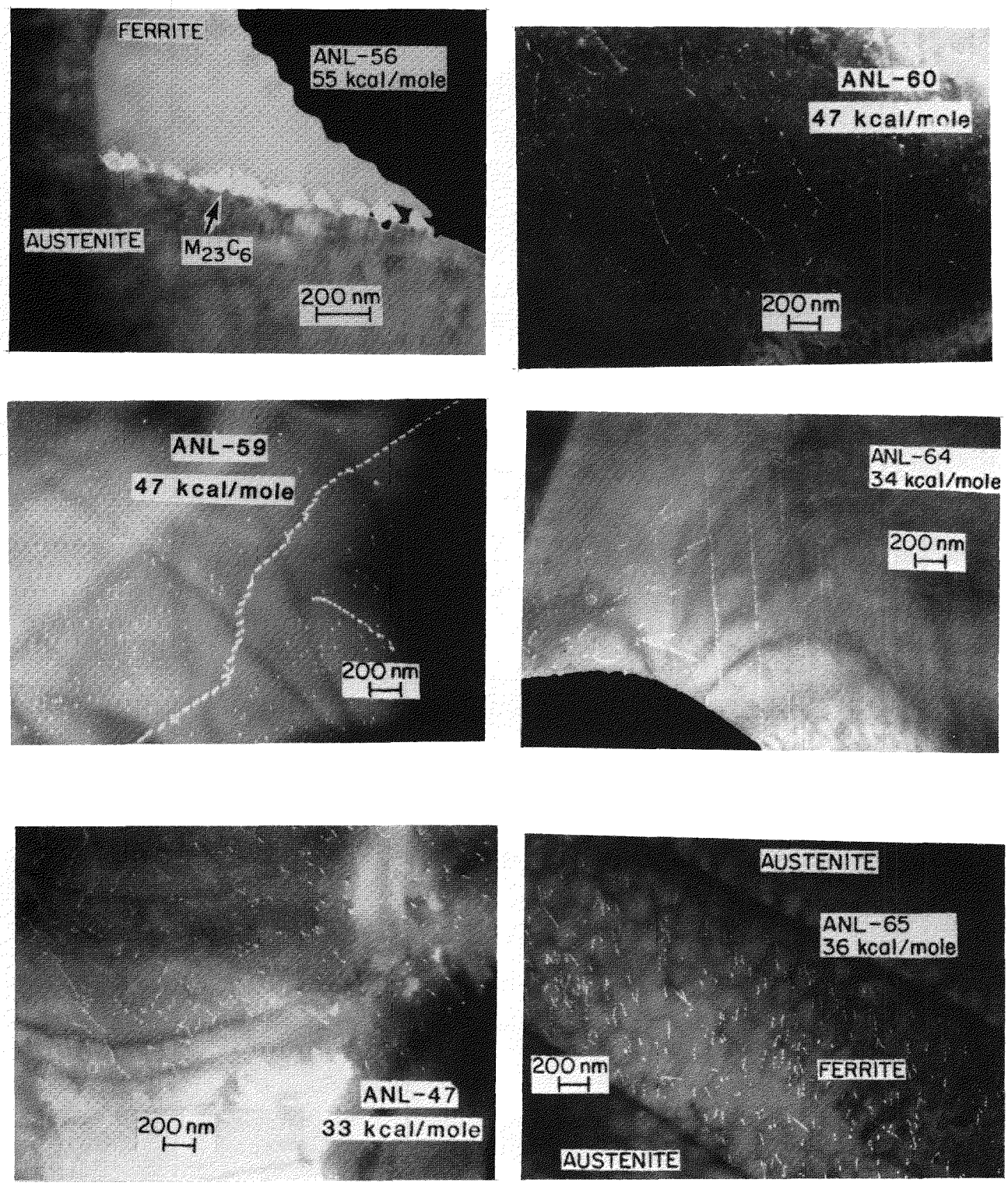

Fig. 2. Dark-Field TEM Morphologies of G-Phase Size and Distribution in Ferrite of Several Heats Observed after Aging at 400°C for 30,000 h. Heat GF-280 was aged for 70,000 h.

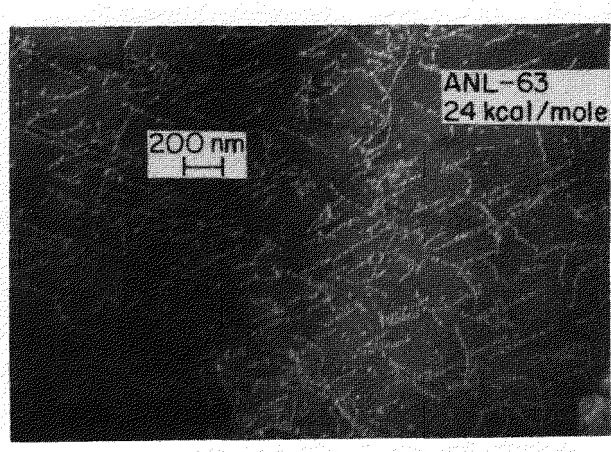
ANL-63
24 kcal/mole
200 nm

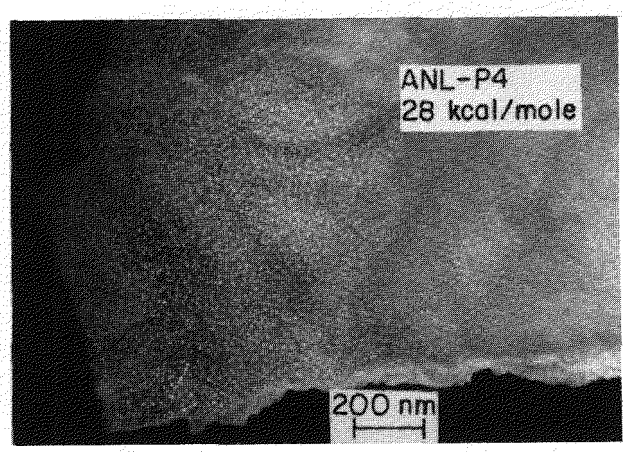
ANL-P4
28 kcal/mole
200 nm

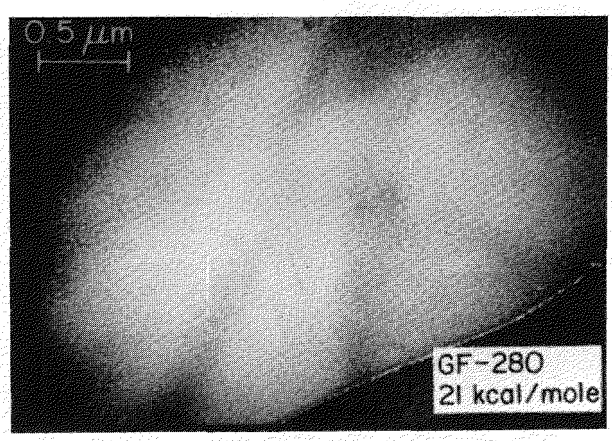
0 5 μm
GF-280
21 kcal/mole

Fig. 2. (Contd.)

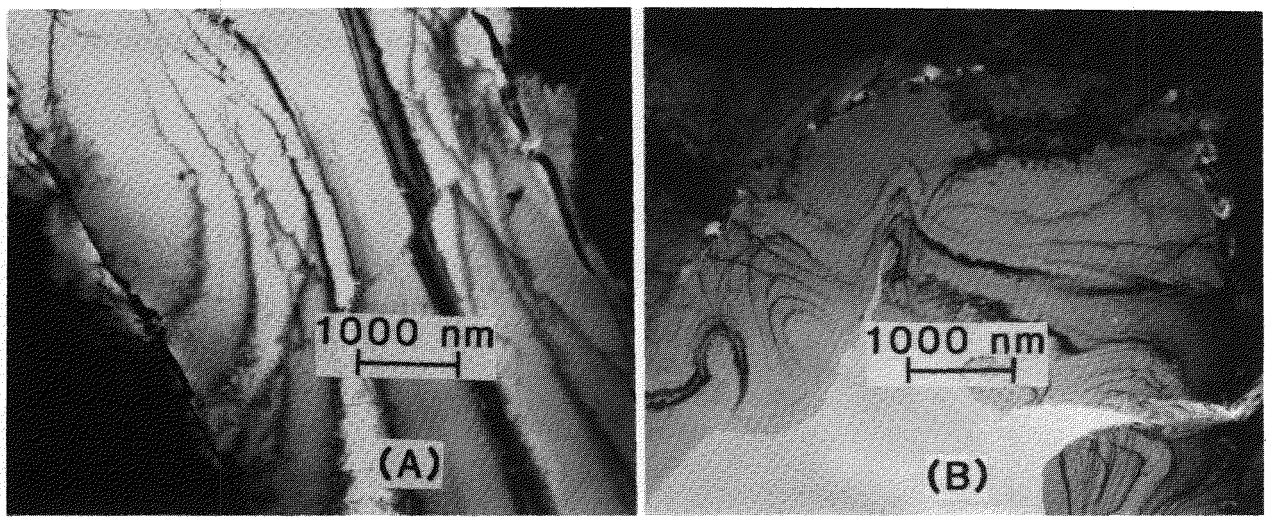

Fig. 3. $M_{23}C_6$ Carbide on Ferrite–Austenite Boundary for Heats 59 (A) and 60 (B), Observed after Aging at 400°C for 30,000 h.

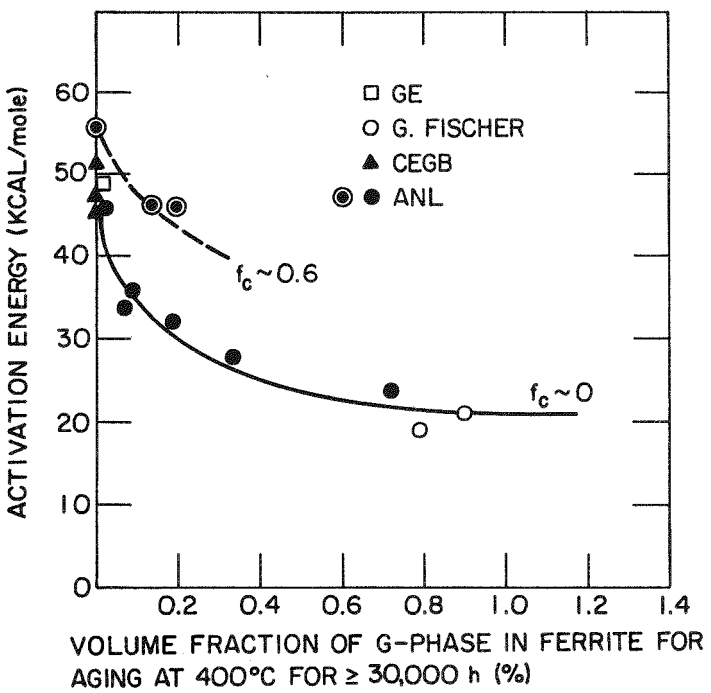

Fig. 4. Activation Energy versus the Volume Fraction of G Phase in Ferrite for Aging at 400°C for ≥30,000 h.

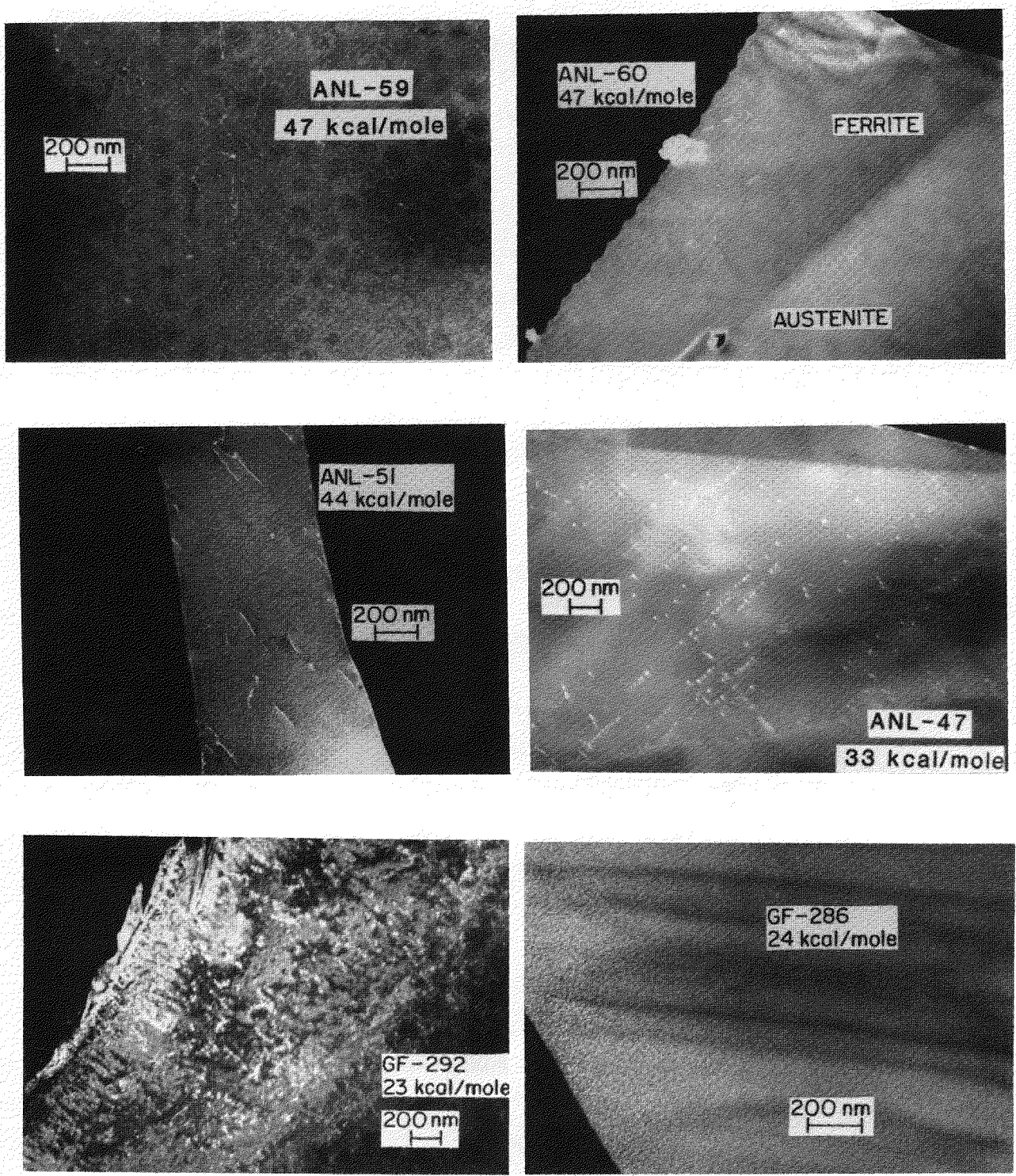

Fig. 5. Dark-Field Morphology of G Phase after Aging at 400°C for 10,000 h.

Table 3. Results of Dark-Field-Imaging Characterization of G-Phase Size, Density, and Volume Fraction in Ferrite of Cast Stainless Steel Heats Aged at 400°C for 30,000 h

Heat	Grade	Aging Test	Activation[a] Energy (kcal/mole)	Overall Composition (wt.%)				Average Diameter of G Phase (nm)	Density of G Phase (10^{21} m^{-3})	G-Phase Volume Fraction (%)
				Mo	Si	Ni	C			
278[b]	CF-8	GF	19	0.13	1.00	8.27	0.038	6	70	0.79
280[b]	CF-8	GF	21	0.25	1.37	8.00	0.028	6	80	0.90
56	CF-8	ANL	56	0.30	1.16	8.93	0.060	5	<0.05	<0.005
63	CF-8M	ANL	24	2.57	0.58	11.85	0.055	12	8	0.72
64	CF-8M	ANL	34	2.46	0.63	9.40	0.038	8	3	0.07
65	CF-8M	ANL	36	2.57	0.48	9.63	0.049	8	4	0.09
P4	CF-8M	ANL	28	2.05	1.02	10.00	0.040	5	50	0.33

[a]From room temperature Charpy-impact tests.
[b]Aged at 400°C for 70,000 h.

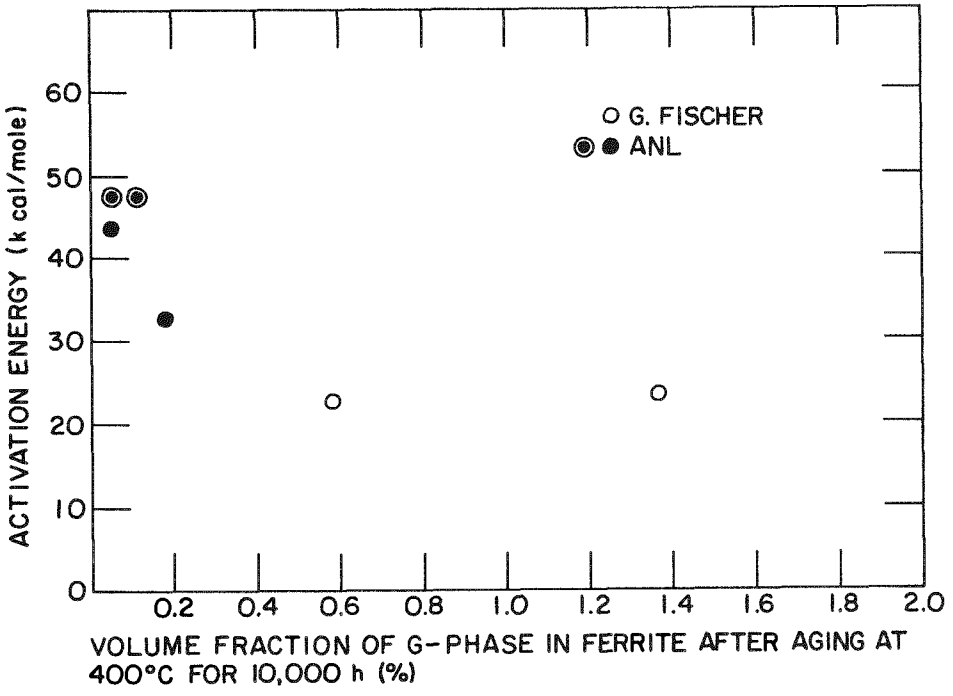

Fig. 6. Activation Energy versus G-Phase Volume Fraction in Ferrite for Aging at 400°C for 10,000 h.

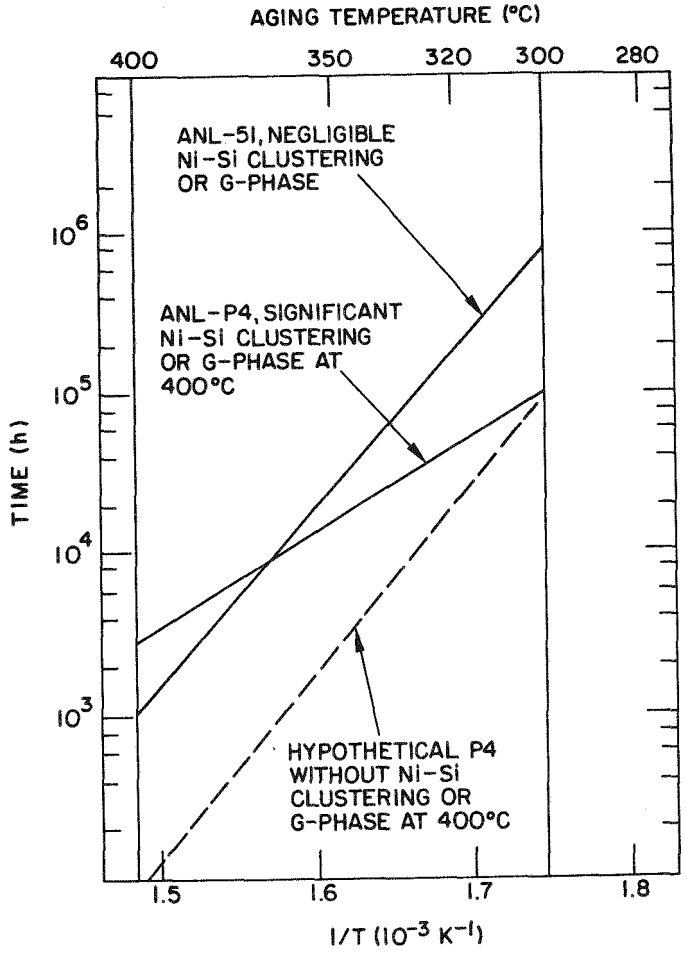

Fig. 7.

Characteristic Aging Time to Reach 50% Impact Energy Drop versus Aging Temperature for Heats 51 and P4, Illustrating the Effect of Microstructure on Activation Energy.

Effect of Ni on the Kinetics of Spinodal Decomposition

In a manner similar to that applied when studying the effect of Ni on the acceleration of the nucleation and growth of the α' precipitates,[18,24] it seems reasonable to postulate that the Ni also accelerates spinodal decomposition of ferrite. In fact, the results obtained in the previous section (i.e., a comparison of Figs. 1 and 4) indicate that "free" Ni atoms in the ferrite (i.e., those not participating in Ni–Si or Ni–Si–Mo clustering, or in G–phase nucleation) promote a faster spinodal decomposition.

Direct evidence that faster spinodal decomposition is associated with a higher level of Ni can be obtained only from materials that have the same chemical composition, other than Ni, and have been aged under identical conditions. For this purpose, a piece of material approximately 15 mm x 10 mm x 5 mm was cut from a hot–leg main valve of the Shippingport reactor, which had been in service for approximately 22 yr. The bulk composition (in wt.%) was as follows: 0.052 C, 0.051 N, 0.24 Si, 0.72 Mn, 0.041 P, 0.011 S, 10.54 Ni, 20.81 Cr, 0.24 Mo, and 10.0% ferrite.[20] Three tips for FIAP analysis were prepared from the material, and the ferrite composition of each tip was determined. The results are given in Table 4.[25] Typically 32,000 to 76,000 field ions from each tip were analyzed to determine the ferrite composition. Fluctuation profiles of Fe and Cr, determined for the three tips by FIAP,[25] are shown in Fig. 9.

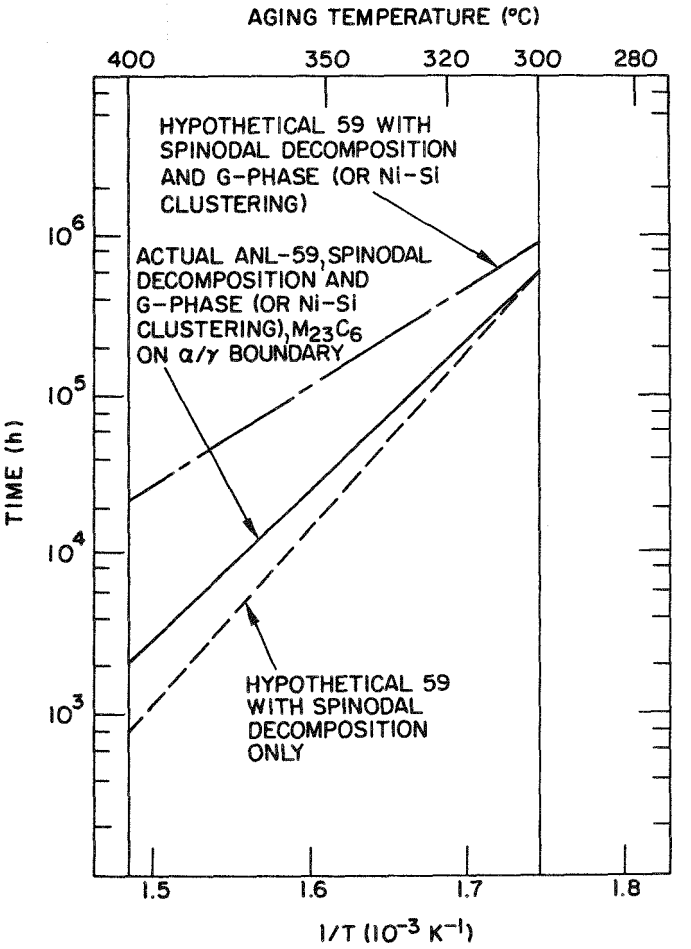

Fig. 8.

Characteristic Aging Time to Reach 50% Impact Energy Drop Versus Aging Temperature for Heat 59, Illustrating the Effect of Microstructure on Activation Energy.

Table 4. Summary of Chemical Composition Analysis by Field Ion Atom Probe[a] of the Ferrite Phase of Specimens from the Main Valve MA9 of the Shippingport Reactor[b]

Specimen Number	Total Number of Ions Analyzed	Ferrite Composition (at.%)						
		Fe	Cr	Ni	Mo	Si	Mn	P
MA9-1	31,737	66.32	21.01	9.70	0.69	0.63	1.48	0.16
MA9-2	76,819	65.92	21.61	9.85	0.65	0.67	1.08	0.21
MA9-3	62,713	65.86	22.97	8.36	0.65	0.67	1.22	0.27

[a]From T. R. Leax, Westinghouse Electric Corp., unpublished work, 1989.
[b]See Ref. 25 for detailed information.

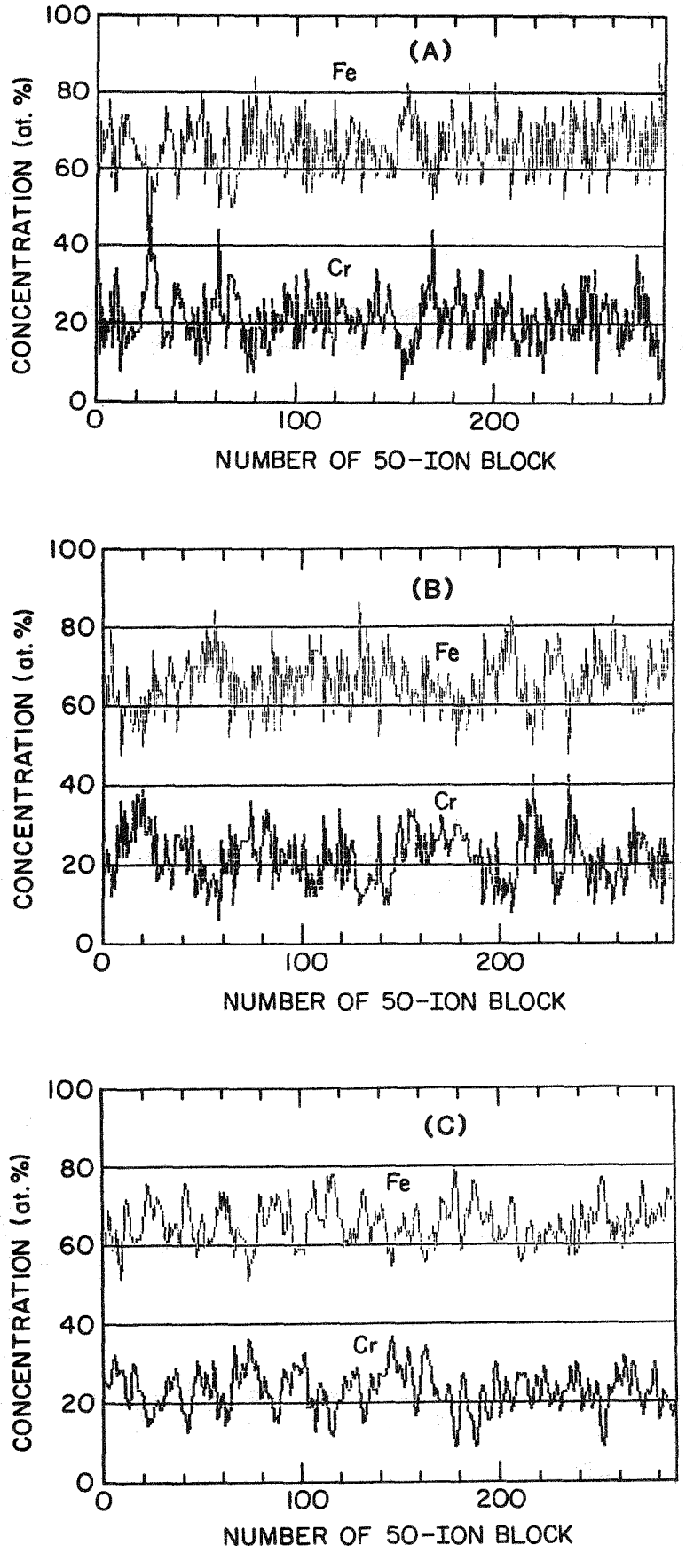

Fig. 9.

Results of FIAP Analysis of the Shippingport PWR Hot-Leg Main-Valve Specimens (Table 4); Fe and Cr Profiles of Specimen MA9-1(A), MA9-2(B), and MA9-3(C).

A comparison of the FIAP profiles shown in Figs. 9A, 9B, and 9C reveals important kinetic information. Although the three specimen tips for FIAP analysis were obtained from a single piece of valve section, the chemical composition of the ferrite phase of each tip was somewhat different (Table 4). The major difference was the Ni content, i.e., 9.70, 9.85, and 8.36 at.%, respectively. The low-Ni specimen MA9-3 (Fig. 9C) showed a relatively less advanced stage of spinodal decomposition than the other two tips. For example, compared to the maximum Cr fluctuation of ~45 at.% observed for the higher Ni specimens, the low-Ni MA9-3 showed a maximum Cr fluctuation of ~37 at.%. Since neither G phase nor Ni-Si clustering was observed,[25] we suggest that under otherwise identical conditions, the lower Ni level in the ferrite matrix produces a slower spinodal decomposition. This observation is consistent with the conclusion reached in the previous section.

Absolute Rate of Aging

In contrast to the activation energy (i.e., a relative rate of aging at temperatures of 400 and 300°C), it was difficult to establish a correlation between the absolute rate of aging (e.g., at 400°C) and microstructural characteristics. This is due primarily to the complexities of the kinetics of the spinodal decomposition and G-phase precipitation, which are influenced by many factors other than Ni, e.g., ferrite content, morphology, and ferrite chemical composition. Given a similar overall chemical composition, the ferrite chemical composition is expected to be influenced by the fabrication process. The absolute rates of aging of the heats included in the analysis of Fig. 4 have been plotted in Figs. 10-12 for comparison. In Fig. 10, schematic aging kinetics at 400 and 300°C are shown in which the characteristic time to reach the mid-level impact energy is defined for the two temperatures. The characteristic aging times t_{400} and t_{300} are convenient parameters that represent the absolute rates of aging at the two temperatures. In Fig. 11, the mid-level impact energy has been plotted as a function of the characteristic aging times of CF-3, CF-8, and CF-8M heats that have been aged in a number of laboratories [i.e., GE, GF, Framatome (FRA), CEGB, and Argonne National Laboratory (ANL)] at 400, 320, and 300°C. The figure shows that the scatter in the absolute rate of aging is similar for the three aging temperatures. For aging at 400°C, the variation (scatter) in the characteristic aging time corresponds to approximately two orders of magnitude. For aging at 300°C, the scatter is also approximately two orders of magnitude. The characteristic times for aging shown in Fig. 11 were normalized for a temperature interval of 300 to 400°C and were plotted in Arrhenius form in Fig. 12. The slope of the line for each heat represents an activation energy.

As pointed out in Ref. 16, most of the GF heats shown in Fig. 12 exhibit an activation energy that is invariably low. The distinct aging behavior of the GF materials may be associated with a number of factors, i.e., fabrication process, additional solution anneal at 1010°C, relatively low Ni and C, and relatively high Si levels. The high level of Si in most of the GF materials promotes more extensive G-phase precipitation, and, as shown in Figs. 8 and 10, this is conducive to a lower activation energy. However, two of the GF heats, i.e., Heats 281 and 282, contain very little Si (0.45 and 0.35 wt.%, respectively, Table 2). Impact energies measured for these two heats show that the kinetics of 300°C aging are relatively slow compared to those of other heats (Fig. 12). The low-Si heats (281 and 282) show activation energies of 33 and 48 kcal/mole, respectively. This is in contrast to the behavior of the rest of the high-Si GF heats, which invariably have low activation energies

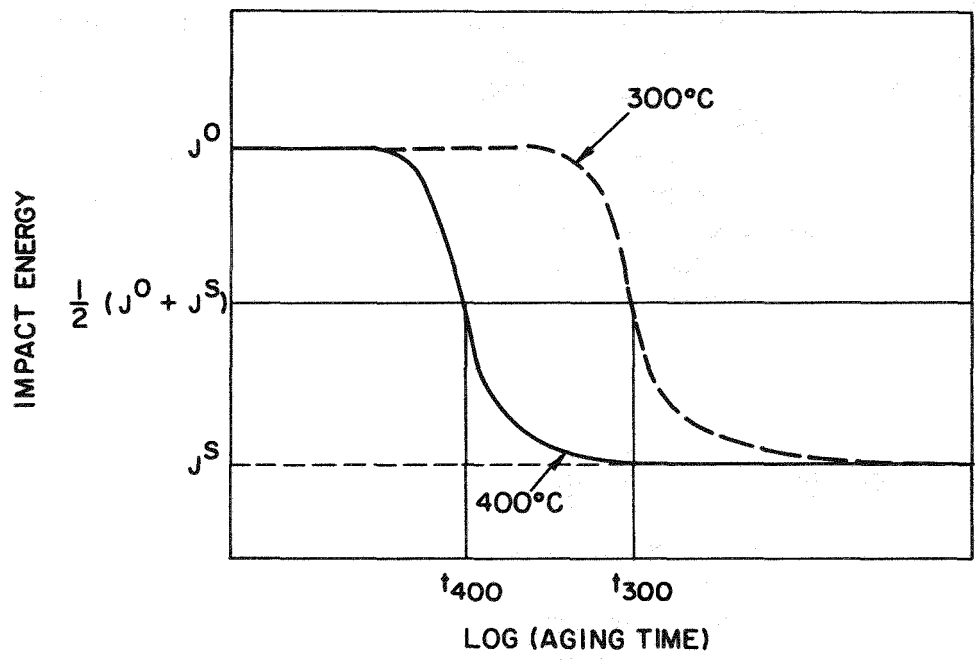

Fig. 10. Definition of Cheracteristic Aging Times to Reach Mid-Level Impact Energy (50% Drop) for 400 and 300°C Aging.

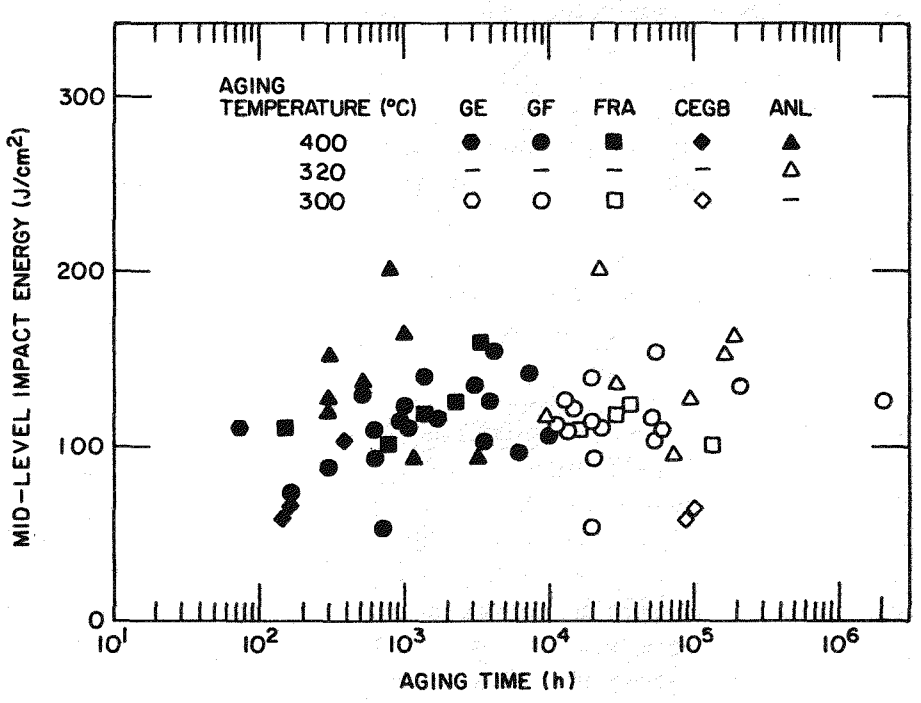

Fig. 11. Mid-Level Impact Energy Versus Characteristic Aging Times for 400, 320, and 300°C Aging for Heats Tested at GE, CEGB, FRA, GF, and ANL.

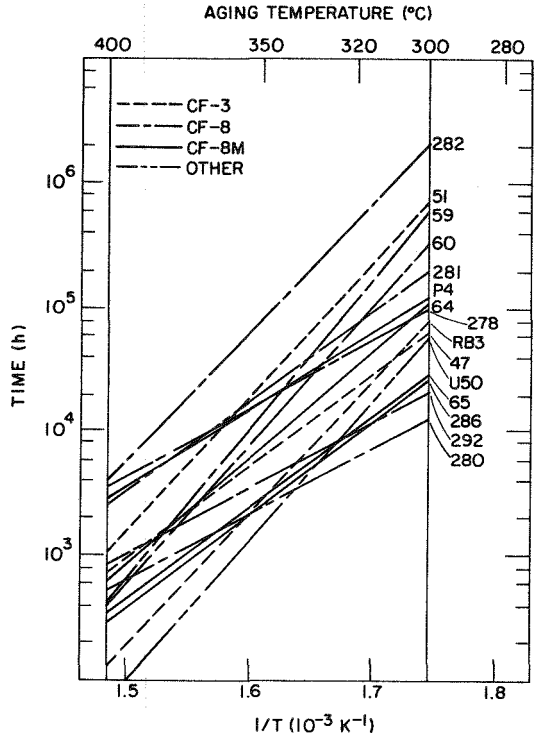

Fig. 12.

Comparison of Characteristic Aging Times for 50% Impact Energy Drop Observed for a Number of Heats of CF-3, CF-8, and CF-8M Stainless Steels.

(18–24 kcal/mole). Since the low-Si levels of Heats 281 and 282 are expected to produce less Ni–Si clustering or G–phase precipitation, the observation tends to provide further support for the validity of the mechanistic model.

Effect of Fabrication Process

The morphology of G–phase precipitates in Figs. 2 and 5 reveals some important characteristics. That is, in contrast to most of the GF heats, some of the ANL heats contained a high density of dislocations in the ferrite phase. G–phase precipitation occurred preferentially on the dislocations in some of the ANL heats, e.g., Heats 64, 65, 63, and 47. This behavior indicates that the activation energy is influenced by dislocation structures, since dislocations promote G–phase nucleation and precipitation. The dislocations in the ferrite apparently are produced during the fabrication process because of mechanical and thermal stresses. Dislocations produced during an impact test will not accompany the G–phase precipitates. Thus, it seems that the fabrication process is an important consideration in evaluating the activation energy of aging.

Another aspect of the fabrication process that may influence the activation energy is the variation in the actual chemical composition of ferrite rather than the bulk composition of the steel. An example of this is given in Table 4 where the variation in Ni content among the nominally identical FIAP tip specimens apparently alters the kinetics of spinodal decomposition (Fig. 9). In general, Ni and Fe atoms are partitioned preferentially in austenite, and, in contrast, Cr, Mo, and Si atoms are preferentially partitioned in ferrite. However, the degree of partitioning of those elements, which is known to influence the kinetics of the spinodal decomposition and G–phase precipitation, is expected to be significantly influenced by the fabrication process. Not much information has been

reported in the literature on the quantitative behavior of the partitioning. Ferrite composition data available from energy dispersive X-ray analysis (EDS)[26,27] and FIAP analyses have been collected and the ferrite partitioning ratio (i.e., ferrite-to-overall chemical composition ratio) has been calculated. The results are summarized in Table 5. Of particular interest in the table are the partitioning ratios of Ni, Si, and Cr, which strongly influence the kinetics of the spinodal decomposition and G-phase precipitation, and hence, the activation energy. Although uncertainty limits of the EDS analysis, in particular for Si, should be considered unacceptable, the results in the table clearly indicate that the partitioning ratios for those elements are significantly influenced by the variation in the fabrication process.

In view of these findings, it seems conclusive that not only the absolute rate of aging but also the activation energy is strongly influenced by the fabrication process. The relationships among the bulk composition, critical factors of the fabrication process, microstructure, and the activation energy of aging are illustrated schematically in Fig. 13.

Conclusions

1. Kinetics of the spinodal decomposition and G-phase precipitation are strongly influenced by nominally small differences in fabrication process and chemical composition, in particular, Ni, Mo, Si, and C. Higher levels of Ni in ferrite matrix appear to accelerate the spinodal decomposition under otherwise identical conditions. The decomposition rate also appears to be influenced strongly by Ni-Si (or Ni-Si-Mo) clustering or nucleation and growth of G phase.

2. It may be difficult to obtain a single empirical correlation of activation energy that can provide a reliable extrapolation of aging behavior regardless of fabrication process and thermomechanical history. However, a mechanistic correlation based on microstructural characteristics was obtained, and it was shown that this correlation provides a good prediction of activation energy regardless of grade, fabrication process, and thermo-mechanical history.

2.2.2 Spinodal-Like Decomposition of Austenite

Introduction

In the previous reporting period, spinodal-like decomposition of austenite was reported for two ANL heats of CF-8M steel containing a relatively high level of Ni, i.e., Heats 63 and P4 (Table 2). In this report, several more heats have been examined to better characterize the behavior after aging at 400, 350, and 320°C. In addition to the previous two heats, the spinodal-like decomposition was observed in CF-3 Heat 47 and CF-8M Heat 65. A summary of the austenite decomposition results is given in Table 6. Further characterization of the decomposed austenite has been conducted by (STEM) and scanning electron microscopy (SEM)-EDS. The results and implications of the analysis are described below.

Table 5. Summary of Ferrite-to-Overall Chemical Composition Ratios (Partitioning Ratio) of Aged Cast Duplex Stainless Steel

Heat No. or Component	Grade	Where Aged[a]	Aging Temp. (°C)	Aging Time (h)	Ferrite Content (%)	Specimen No.	Ferrite/Bulk Partitioning Ratio							Analysis[b] Technique	Reference[c]
							Fe	Cr	Ni	Mo	Si	Mn	P		
L	CF-8M	FRA	400	7,500	17.5	L-01	0.95	1.29	0.60	1.64	1.91	–	–	EDS	26
						L-02	0.95	1.27	0.57	1.66	2.53	–	–	EDS	26
						L-03	0.94	1.28	0.60	1.92	1.23	1.01	–	EDS	27
278	CF-8	GF	400	70,000	15.0	278-A	0.94	1.41	0.45	2.77	1.42	0.28	–	EDS	27
Hot-Leg Main Valve	CF-8	Shippingport PWR	Reactor	~22 yr	10.0	MAC-10	0.98	1.31	0.54	0.78	0.40	–	–	EDS	d
						MAC-1	0.99	0.95	0.98	4.92	1.34	2.05	2.19	FIAP	d
						MAC-2	0.99	0.98	0.99	4.64	1.42	1.50	2.87	FIAP	d
						MAC-3	0.99	1.04	0.84	4.64	1.42	1.69	3.70	FIAP	d
Pump Volute	CF-8	Shippingport	Unaged	Unaged	16.2	VRC-10	0.98	1.24	0.64	–	0.96	–	–	EDS	d
Y4331	CF-8MC	FRA	400	700	20.0	4331-A	0.96	1.20	0.72	1.68	1.31	0.26	–	EDS	e
						4331-B	0.93	1.14	0.76	2.48	1.62	1.56	–	FIAP	e
Y3296	CF-8MC	FRA	400	8,000	33.0	3296-A	0.96	1.18	0.81	1.61	1.20	0.15	–	EDS	e
						3296-B	0.95	1.09	0.89	1.95	1.29	1.66	–	FIAP	e

[a]FRA = Framatome, GF = Georg Fischer Co.
[b]EDS = Energy-Dispersive X-ray Analysis, FIAP = Field Ion Atom Probe.
[c]Source reference of EDS or FIAP analysis.
[d]T. R. Leax, Westinghouse Electric Corp., unpublished work, 1989.
[e]T. R. Leaux, S. S. Brenner, and J. A. Spitznagel, "Atom Probe Analysis of Thermal Aging Effects on Cast Stainless Steel," Westinghouse Electric Corp., unpublished work, 1987.

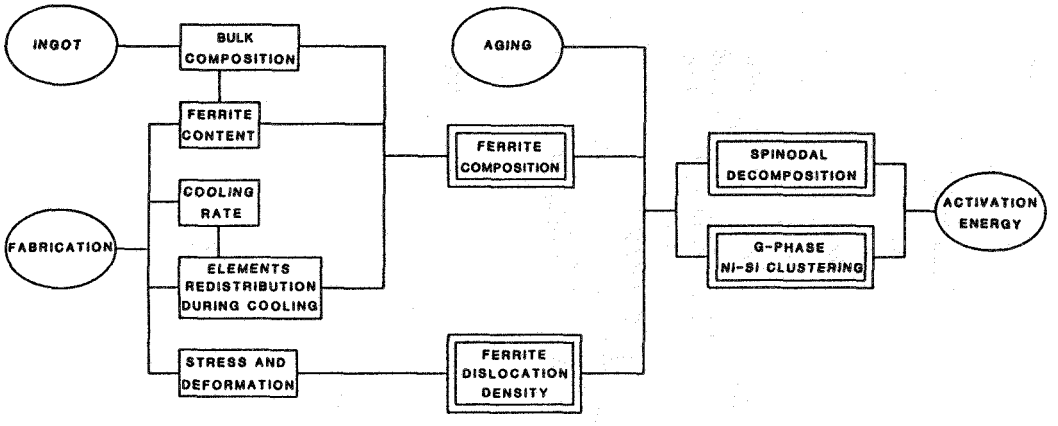

Fig. 13. Schematic Illustration of the Influence of Fabrication Process and Microstructural Evolution on the Activation Energy of Aging.

Table 6. Chemical Compositions of Several Heats of CF-3, CF-8, and CF-8M Cast Duplex Stainless Steels Selected for Characterization of Austenite Decomposition

Heat No.	Grade	Composition (wt.%)							Ferrite Content (%)	Austenite Decomposition Observed[a]
		Mn	Si	Mo	Cr	Ni	N	C		
47	CF-3	0.60	1.06	0.59	19.81	10.63	0.028	0.018	16.3	Yes
56	CF-8	0.60	1.16	0.30	19.33	8.93	0.030	0.060	10.1	No
59	CF-8	0.60	1.08	0.32	20.33	9.34	0.045	0.062	13.5	No
63	CF-8M	0.61	0.58	2.57	19.37	11.85	0.031	0.055	10.4	Yes
P4	CF-8M	1.07	1.02	2.05	19.64	10.00	0.151	0.040	10.4	Yes
64	CF-8M	0.60	0.63	2.46	20.76	9.40	0.038	0.038	28.4	No
65	CF-8M	0.50	0.48	2.57	20.78	9.63	0.064	0.049	23.4	Yes
278[b]	CF-8	0.28	1.00	0.13	20.20	8.27	0.027	0.038	15.0	No[c]
280[b]	CF-8	0.50	1.37	0.25	21.60	8.00	0.029	0.028	38.0	No[c]

[a]After thermal aging at 400, 350, and 320°C for 30,000 h (3.4 yr).
[b]Obtained from G. Fischer Co. of Switzerland.
[c]After aging at 400, 350, and 300°C for 70,000 h (8 yr).

Results of TEM, EDS Characterization

Specimens from the heats listed in Table 6 have been examined by TEM after long-term aging at 400, 350, and 320°C for 10,000 h (1.1 yr), 30,000 h (3.4 yr), and, in the case of Heats 278 and 280, for 70,000 h (8 yr). For Heat 47, 63, 65, and P4, austenite morphologies indicated a decomposition that occurred during aging for 30,000 h. Those heats contained a higher Ni content in the bulk specimens than the other five heats, which did not show any decomposition in the austenite phase, i.e., 9.63 to 11.85 wt.% vs 8.00 to 9.40 wt.%. The Ni content in austenite is 1.1 to 1.3 times higher than the bulk composition. Bright-field morphologies of the decomposed regions of austenite are shown in Fig. 14 for the four heats. Ferrite and austenite boundaries are visible in the figure for Heats 47, 63, and P4. In the austenite grain, near the ferrite in particular, nearly spherical or elliptical regions of light contrast several hundred nanometers in size are visible in high density. Similar regions of light contrast but of a more irregular shape are visible for Heat P4, which appears to be in a more advanced stage of decomposition than the other heats despite the lower aging temperature (i.e., 350 vs 400°C). The diffraction patterns corresponding to the decomposed regions of Fig. 14 did not show any reflections other than austenite, indicating that no other second phase is present in the austenite. The light and dark contrast in the austenite indicates an inhomogeneity in the austenite either in local chemical composition or in thickness on a fine scale, or both. Features essentially identical to those of Fig. 14 have been observed for irradiated Fe-Ni alloys and were termed "worm-holes".[28] They apparently are caused by nonuniform chemical attack of the local region during jet thinning as a result of a nonuniform chemical composition. The worm-hole morphologies were observed in some but not all of the TEM specimens from each heat after identical aging. This indicates that the reaction was uneven.

Morphologies shown in Fig. 15 for Heat P4 indicate the effect of temperature on the kinetics of decomposition after aging for 30,000 h at 400, 350, and 320°C. For this particular heat, the reaction is apparently fastest at 350°C. At 320°C, the reaction was observed only on the austenite-austenite grain boundaries, Fig. 15(C). Similar morphology has also been observed in Heat 63 specimens after aging at 320°C for 30,000 h.

The results of STEM-EDS analysis of the decomposed austenite regions are shown in Figs. 16 and 17. EDS profiles for the two circled spots of Fig. 16(A), spots on and away from the light-contrast feature, are shown in Fig. 16(B) as the solid and dotted peaks, respectively. Ratios for the peak heights (i.e., solid-to-dotted peak ratios) measured from Fig. 16(B) are: Fe, 0.66-0.70; Cr, 0.62; Ni, 0.62-0.63; Si, 0.67; and Mo, 0.73. This indicates a slight depletion of Ni and Cr for the lightly contrasted spot compared to the austenite matrix. This is consistent with similar observations made for neutron-irradiated Fe-Ni and Fe-Ni-Cr.[30] That is, the localized regions, relatively low in Ni, are preferentially attacked by the jet-thinning solution, and, as a result, relatively thin local regions (and in some cases, perforations) are produced [Fig. 14(A)].

In addition to the Ni-depleted, lightly contrasted regions of Fig. 16, dark bands, reported to be relatively rich in Ni from the investigation of the irradiated Fe-Ni and Fe-Ni-Cr alloys,[28] have also been observed in the present study. Morphology and EDS analysis of the dark bands are shown in Fig. 17. In the figure, EDS profiles from the dark band and from a lightly contrasted spot away from the dark band are compared. Ratios for the peak heights (i.e., ratio of dark band to matrix) measured from Fig. 17(B) are: Fe, 0.68; Cr, 0.75;

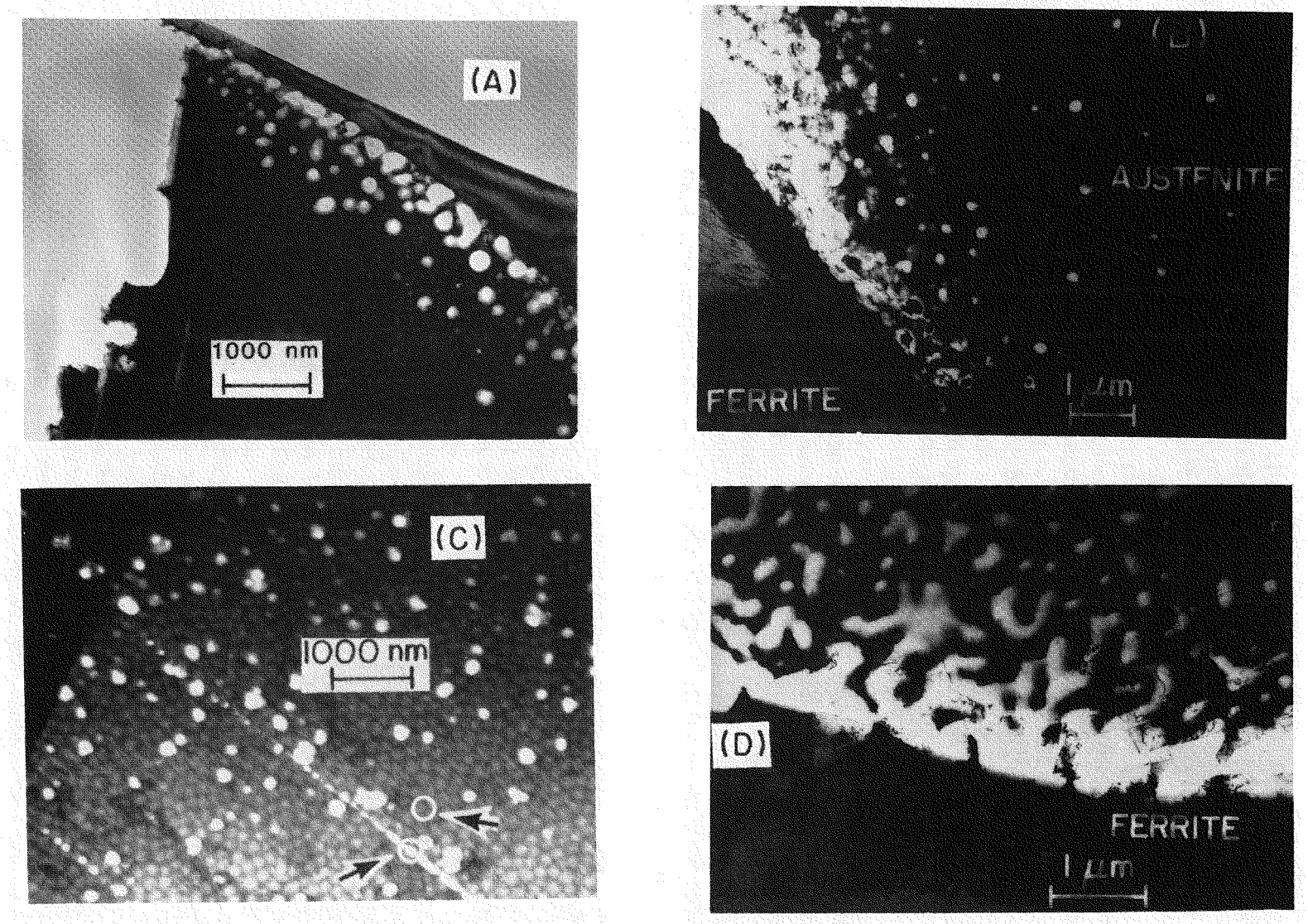

Fig. 14. TEM Bright-Field Morphologies of Decomposed Austenite of Cast Duplex Stainless Steels after Aging for 30,000 h (3.4 yr).

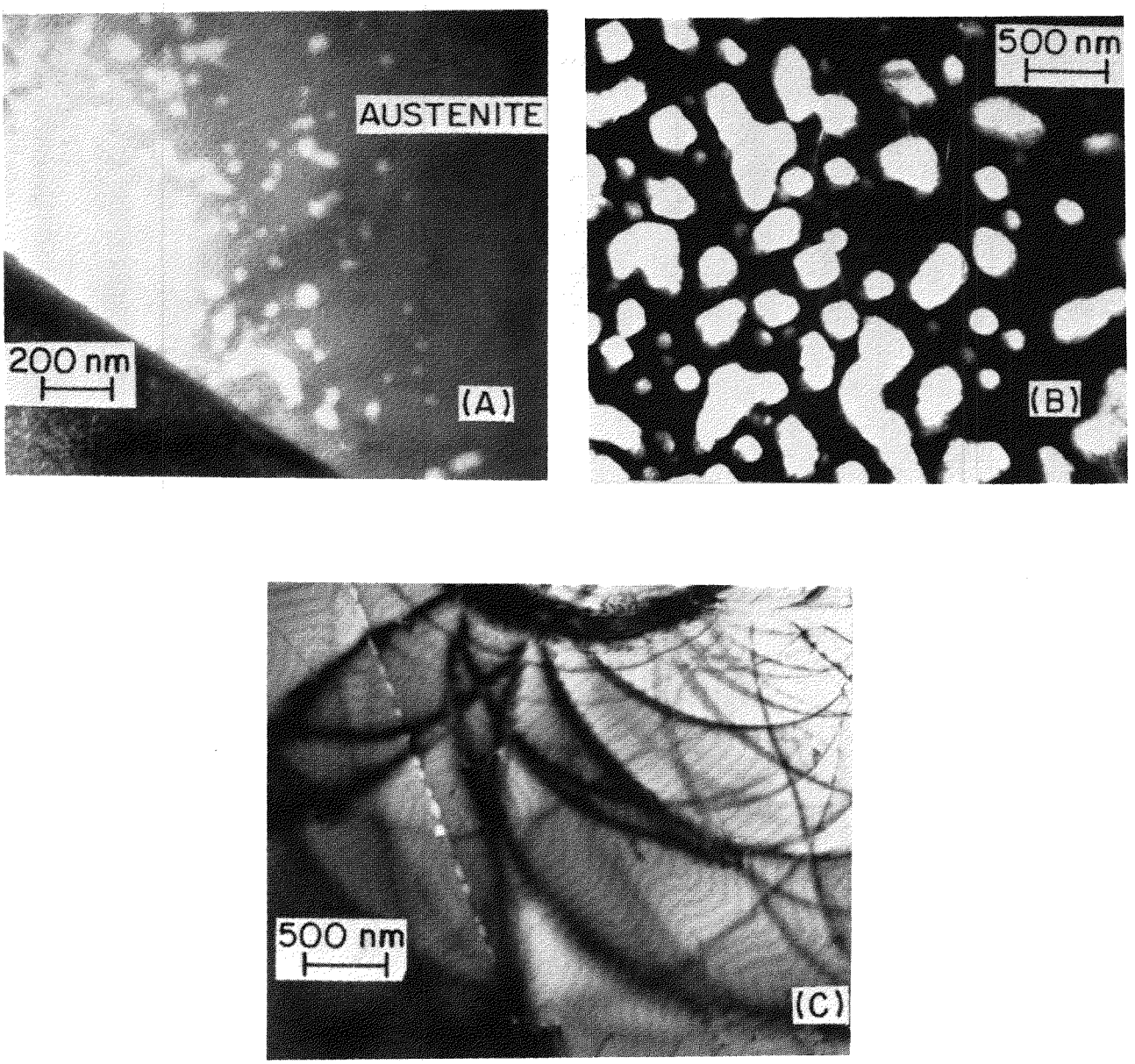

Fig. 15. TEM Bright-Field Morphologies of the Spinodal Decomposition of Austenite of Heat P4 after Aging for 30,000 h at (A) 400°C, (B) 350°C, and (C) 320°C.

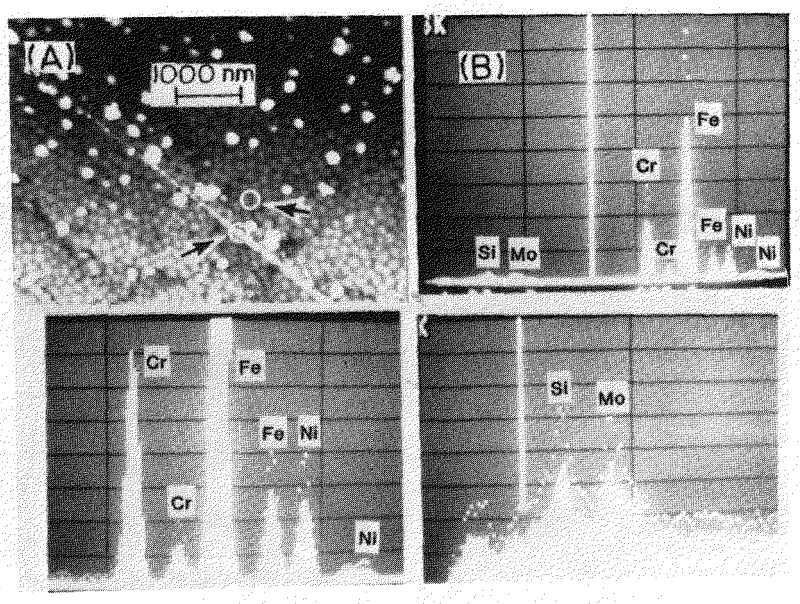

Fig. 16. STEM–EDS Profiles of Decomposed Austenite Regions [Circled Spots in (A)] on [EDS Signal, Solid Peaks (B)] and Away from [EDS Signal, Dotted Peaks (B)] the Linear Feature of Light Contrast Shown in Bright-Field Image (A).

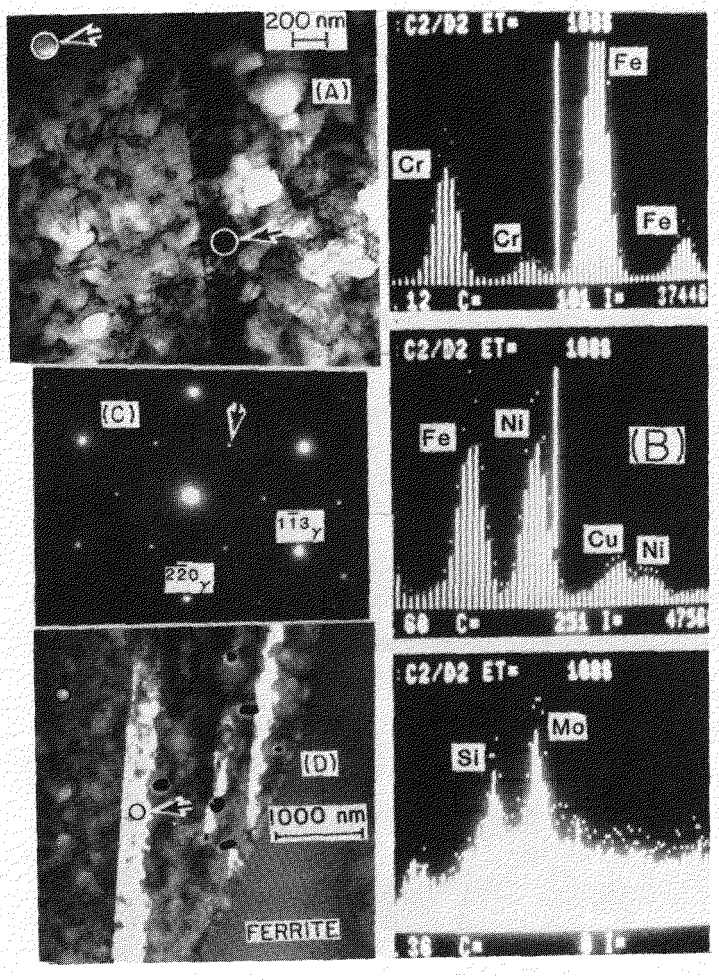

Fig. 17.

STEM–EDS Profiles of Decomposed Austenite Regions [Circled Spots in (A)] on the Dark Band [EDS Signal, Solid Bar (B)] and on the Lightly Contrasted Region Away from the Dark Band [EDS Signal, Dotted (B)]; (C), Selected Area Diffraction Pattern, (D), Dark-Field Morphology of the Dark Bands of (A).

Ni, 0.75; Si, 0.826; and Mo, 0.86. This shows that the dark bands are slightly rich in Ni. This is again in agreement with the observation of Garner et al. in which Ni-rich zones containing grain boundaries were identified in irradiated Fe-35Ni and Fe-35Ni-7.5Cr alloys.[28]

Selected-area diffraction patterns [Fig. 17(C)] and dark-field morphology [Fig.-17(D)] of the dark bands of Fig. 17(A) indicate that they are a Ni-rich second phase that exhibits a sharp phase boundary from the austenite matrix. The diffraction pattern of Fig. 17(C) corresponds to an fcc (or slightly tetragonal) FeNi structure where lattice spacing is nearly identical to that of austenite. In the ordered state of the FeNi structure, planes of Fe and Ni atoms alternate in the c-axis of the unit cell, and, as a result, superlattice reflections are expected in addition to the usual austenite reflections. The structure factor F for reciprocal lattice (hkl) of the ordered structure is given by

$F = 0$, for mixed hk

$F = 2\,(f_{Fe} + f_{Ni})$, for unmixed hkl

$F = 2\,(f_{Fe} - f_{Ni})$, for even hk and odd l, or odd hk and even l,

where f_{Fe} and f_{Ni} are the Fe and Ni atomic scattering factors. Apparently, the superlattice reflections are not intense enough in Fig. 17(C) to be visible, indicating that the structure $Fe_{1+x}Ni_{1-x}$ is only partially ordered at best and the nonstoichiometric parameter x is fairly large. The invisible superlattice reflections may also be due to the very close values of f_{Fe} and f_{Ni}. A fully ordered FeNi structure has been reported for the Santa Catharina meteorite, whose composition is close to Fe-35Ni-0.2P in wt.%.[29,30] It appears that the formation of a fully ordered stoichiometric FeNi structure is difficult in the present duplex stainless steels in which the Ni content of the austenite is rather low, i.e., 12-15 wt.%.

Discussion

As reported previously, it seems that only localized regions of the austenite reached an advanced stage of the spinodal-like decomposition in the specimen shown in Fig. 14(D), resulting in a localized hardening of the material.[16] TEM and EDS analyses of the localized hardened region could not be conducted. Whether the ordered FeNi phase is associated with the hardened region, as in the case of the meteorite decomposition, is not clear.

Despite the localized hardening of the austenite, the overall material toughness of the specimen of Fig. 14(D) did not show excessive degradation compared with other heats of similar compositions for similar aging conditions. This is probably because the overall embrittlement was influenced primarily by the faster spinodal decomposition of ferrite, and the austenite decomposition did not advance to produce a significant amount of hardened regions in the austenite. The specimen shown in Fig. 14(D) apparently achieved an advanced stage of decomposition, and yet showed a room temperature impact energy of 55-70-J/cm^2. This is within the range of values expected under similar aging conditions of other heats in which austenite decomposition was absent.[16]

The aging produced at the time and temperature for the most advanced decomposition (i.e., Heat P4 aged at 350°C for 30,000 h) can be compared with the aging expected near the end-of-life of a reactor operation. This requires information on the activation energy of the austenite decomposition near the temperature range of extrapolation. Since the information is not available, a value of ~50 kcal/mole was assumed, i.e., a value similar to the activation energy of spinodal decomposition of ferritic Fe-Cr alloys. In Fig. 18, extrapolations of the aging conditions of Fig. 15 were made to reactor operating temperatures of 320 and 280°C. Assuming an activation energy of 50 kcal/mole, a decomposition similar to that of Fig. 15(B) would be expected for aging at 320°C for 23 yr. The end-of-life aging (i.e., 32 yr at 320°C) would correspond to an aging at 350°C for 42,000 h (4.8 yr).

At this time, it is difficult to predict how significant austenite decomposition might be in relation to the overall material toughness at the end-of-life or life extension situations for nuclear reactors. It seems important to gain a better understanding of the nature of the localized embrittlement reported in Fig. 14 of Ref. 16. If the embrittlement is associated with the formation of an FeNi ordered phase (as in the case of the findings in meteorites), and the rest of Ni-depleted zone in austenite is ductile, an equilibrium volume fraction of the embrittled zone in austenite can be calculated on the basis of the Ni content of the austenite. Information to be obtained from specimens aged for longer times (e.g., 50,000 h) will be helpful to understand the end-of-life material performance.

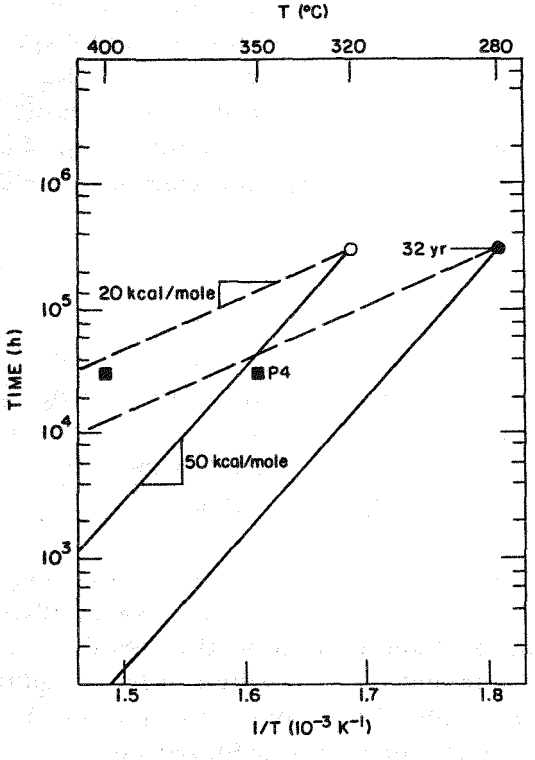

Fig. 18.

Time-Temperature Arrhenius Plot Comparison of the Aging Conditions of the Decomposed Austenite of Heat P4 (3.4 yr at 400 and 350°C) and End-of-Life Reactor Components (32 yr at 320-280°C).

Conclusions

1. Spinodal-like decomposition of the austenite phase in CF-8 and CF-8M-grade cast duplex stainless steels has been observed after long-term thermal aging at 400 and 350°C for 30,000 h (3.4 yr). At 320°C, the reaction was observed only at the limited region near

the austenite grain boundaries. Ni segregation and "worm-holes" corresponding to the spatial microchemical fluctuations have been confirmed. This finding shows the existence of a miscibility gap in the austenite phase of the duplex material. The decomposition was observed only for heats containing a relatively high overall Ni content (9.6–12.0 wt.%) but not in low-Ni (8.0–9.4 wt.%) heats.

2. In some specimens showing a relatively advanced stage of decomposition, localized regions of austenite had a Vickers hardness of 340–430. However, the effect of the austenite decomposition on the overall material toughness appears secondary compared with the effect of the faster spinodal decomposition in the ferrite phase for aging up to 3-5 yr. Effects on the material toughness after longer term aging for end-of-life or life-extension situations of reactors are difficult to predict at this time.

3. The present observation of the thermally driven spinodal-like decomposition of the austenite phase in cast duplex stainless steels validates the proposition that a miscibility gap occurs in Fe-Ni and ancillary systems.

3 Mechanical Properties (O. K. Chopra)

3.1 Introduction

The data from Charpy-impact tests on 11 experimental and 5 commercial heats of cast stainless steel aged up to 10,000 h at 450, 400, 350, 320, and 290°C were presented earlier.[8,9,15,16] The tests were conducted on standard Charpy V-notch specimens according to ASTM specification E 23. A Dynatup Model 8000A drop-weight impact machine with an instrumented tup and a data readout system was used for the tests. The results indicate that thermal aging decreases the impact energy and shifts the transition curve to higher temperatures. Different heats exhibit different degrees of embrittlement. In general, the low-C CF-3 cast materials are the most resistant, and the Mo-containing CF-8M materials are least resistant to embrittlement. For cast materials of all grades, the extent of embrittlement increases with an increase in ferrite content.

The high-C CF-8 or CF-8M steels exhibit low lower-shelf energy and high mid-shelf transition temperature relative to the CF-3 steels because of the formation of $M_{23}C_6$ carbides at the ferrite/austenite phase boundaries. The carbides form either during the production heat treatment of the casting or during aging, particularly at temperatures >350°C. The presence of large carbides weakens the phase boundaries, and the fracture mode is predominantly phase boundary separation. Furthermore, thermal aging leads to a decrease in the ferrite content of cast stainless steel of all grades, Fig. 19; in particular after aging at 450°C. The decrease in ferrite content is significantly greater in CF-8M steels than in steels of other grades. These results indicate that data obtained at 450°C may not be representative of reactor operating conditions; material aged at 450°C shows significant precipitation of phase boundary carbides and a reduction in the ferrite content of the steel.

The transition curves for aged cast materials indicate a "saturation" effect for the upper-shelf energy (USE). The values of USE decrease significantly after a relatively short aging time, e.g., ~3000 h at 400°C, and do not change for longer aging times. The decrease

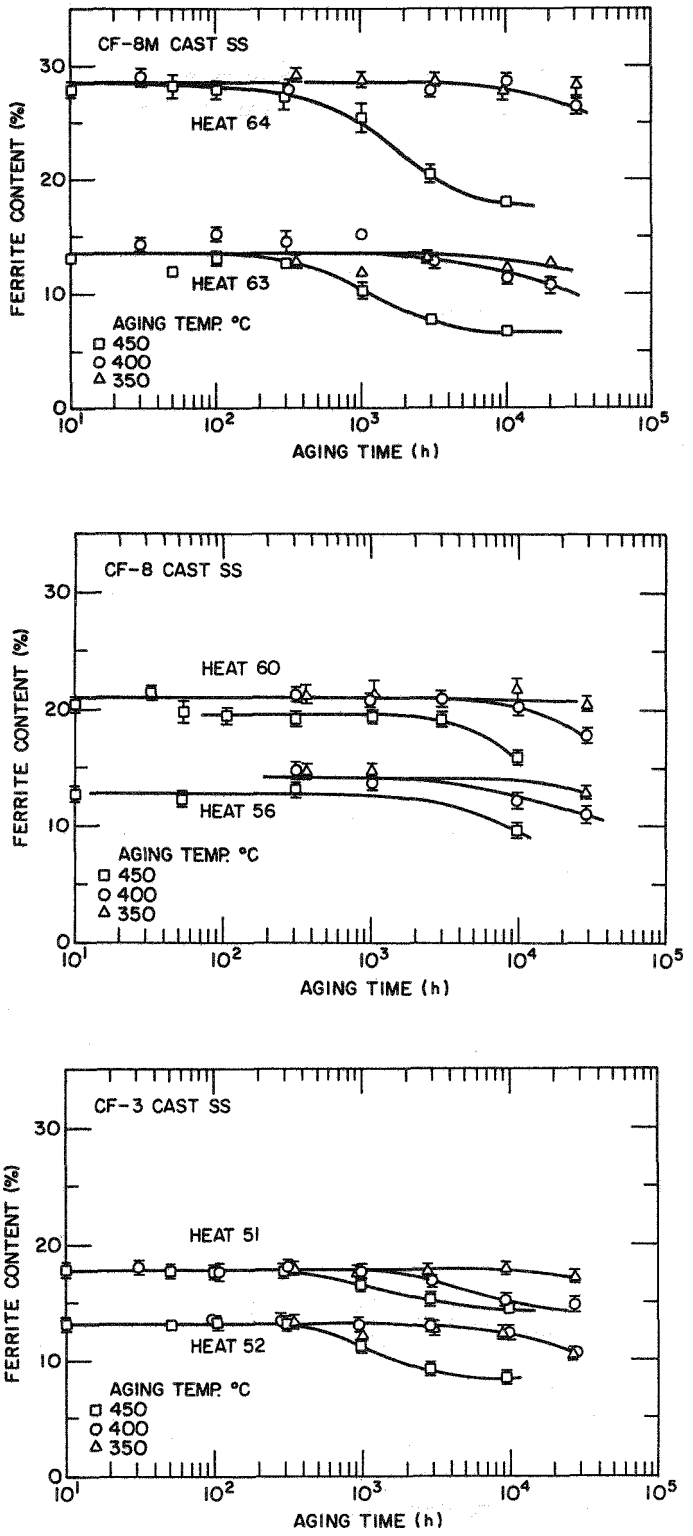

Fig. 19. Decrease in Ferrite Content of Thermally Aged CF-8M, CF-8, and CF-3 Cast Stainless Steel.

in USE, however, depends on the aging temperature, and is greater at higher aging temperatures.

The results also indicate that the current estimates of embrittlement are not valid for all heats of cast stainless steel. The degree of embrittlement at reactor operating temperatures is estimated from Arrhenius extrapolations of laboratory data obtained at higher temperatures.[4] The aging time required to reach a given degree of embrittlement at different temperatures is determined from the equation

$$t = 10^P \exp\left[\frac{Q}{R}\left(\frac{1}{T} - \frac{1}{673}\right)\right], \qquad (1)$$

where Q is the activation energy, R the gas constant, T the absolute temperature, and P the aging parameter that represents the degree of aging reached after 10^P h at 400°C. The activation energy for the process of embrittlement has been described as a function of the chemical composition of the cast material.[7] Thus,

$$Q(\text{kcal/mole}) = -43.64 + 4.76(\%\ \text{Si}) + 2.65(\%\ \text{Cr}) + 3.44(\%\ \text{Mo}). \qquad (2)$$

The activation energy for the process of embrittlement ranges between 60 and 105 kJ/mole (14 and 25 kcal/mole) for the CF-3, CF-8, and CF-8M cast stainless steels. For a specific heat of cast stainless steel, Eqs. (1) and (2) are used to determine the aging conditions that are representative of reactor service. For a cast material with an activation energy of 100 kJ/mole (24 kcal/mole), the end-of-life conditions for cold-leg (i.e., 40 yr at 290°C) and hot-leg (i.e., 40 yr at 320°C) piping are equivalent to 10,000 and 30,000 h at 400°C, respectively. However, estimates from Eqs. (1) and (2) do not accurately represent the Charpy-impact data obtained in the present study.[16]

3.2 Technical Progress

3.2.1 Charpy-Impact Tests

The data for room temperature impact energy were analyzed to determine the kinetics and extent of embrittlement. The Charpy–impact energy KCV is expressed as

$$KCV = K_m + \beta\{1 - \tanh[(P - \theta)/\alpha]\}, \qquad (3)$$

where P is the aging parameter defined in Eq. (1), K_m is the minimum impact energy reached after long–term aging, β is half the maximum decrease in impact energy (i.e., half the difference between initial and minimum impact energy), θ is the log of the time to achieve β reduction in impact energy, and α is a shape factor representing the time between the start and end of the decrease in impact energy.

The values of the constants in Eqs. (1) and (3) for various heats of cast stainless steel are given in Table 7 and the best fit curves for some of the heats are shown in Figs. 20-22. The Charpy–impact data are plotted as a function of the aging parameter in Figs. 23-25.

Table 7. Values of the Constants Representing the Kinetics of Embrittlement for Cast Stainless Steel

Heat	Constants				Activation Energy, kJ/mole (kcal/mole)
	K_m, J/cm^2	β, J/cm^2	θ	α	
47	163.6	38.5	2.89	1.11	91.6(21.90)
51	153.0	31.0	3.06	0.58	184.3(44.06)
56	100.4	51.3	4.22	1.05	234.5(56.05)
59	91.2	63.5	3.26	1.55	196.4(46.94)
60	64.7	63.9	2.82	0.63	198.8(47.51)
63	140.2	58.4	2.43	0.92	101.7(24.30)
64	53.3	73.9	2.47	0.66	142.5(34.06)
65	54.3	78.9	2.84	1.07	152.3(36.39)
66	94.9	74.9	2.72	1.73	125.5(30.23)

The actual time and temperature of aging are shown on five separate axes below the figures. The service time, in years, at the hot-leg temperature of LWRs is shown at the top of the figure.

The results indicate that the kinetics of embrittlement vary significantly for the various heats of cast stainless steel; the activation energies range between 90 and 235 kJ/mole (20 and 56 kcal/mole). The activation energy is lower for the Mo-containing CF-8M steels or for steels with higher Ni content. The values of activation energy obtained in the present study are significantly higher than those observed in the GF study,[4] e.g., activation energies between 70 and 105 kJ/mole (17 and 25 kcal/mole).

3.2.2 Extent of Embrittlement

The Charpy-impact data were analyzed to obtain a correlation between material variables and the extent of embrittlement, i.e., minimum impact energy K_m, that would ever be achieved after long-term aging. The minimum impact energy is plotted in Fig. 26 as a function of a material parameter consisting of the measured ferrite content (δ_m in %); Cr, Mo, Si, C, and N content (in wt.%) of the steel; and the mean ferrite spacing ($\bar{l}$ in μm). The results for all heats for which the material variables were known are shown in the figure. The data show a good correlation with the material parameter. The impact energy for the FRA Heat 4331 (Ref. 31), however, is significantly lower than that predicted from Fig. 26. This heat contained large Nb carbides at the phase boundaries. The fracture surfaces of the impact test specimens

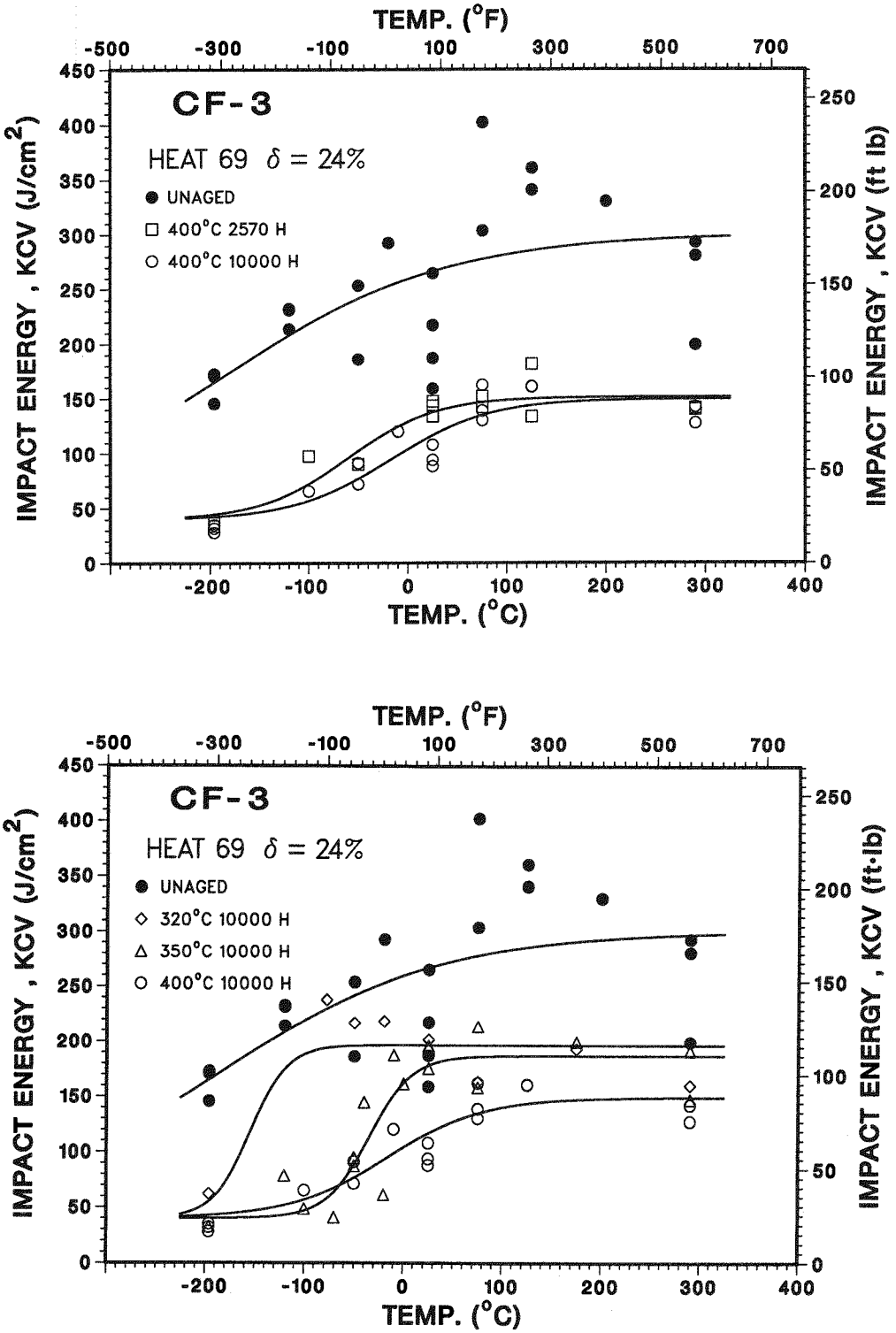

Fig. 20. Effect of Aging Time and Temperature on the Room Temperature Impact Energy of CF-3 Cast Stainless Steel.

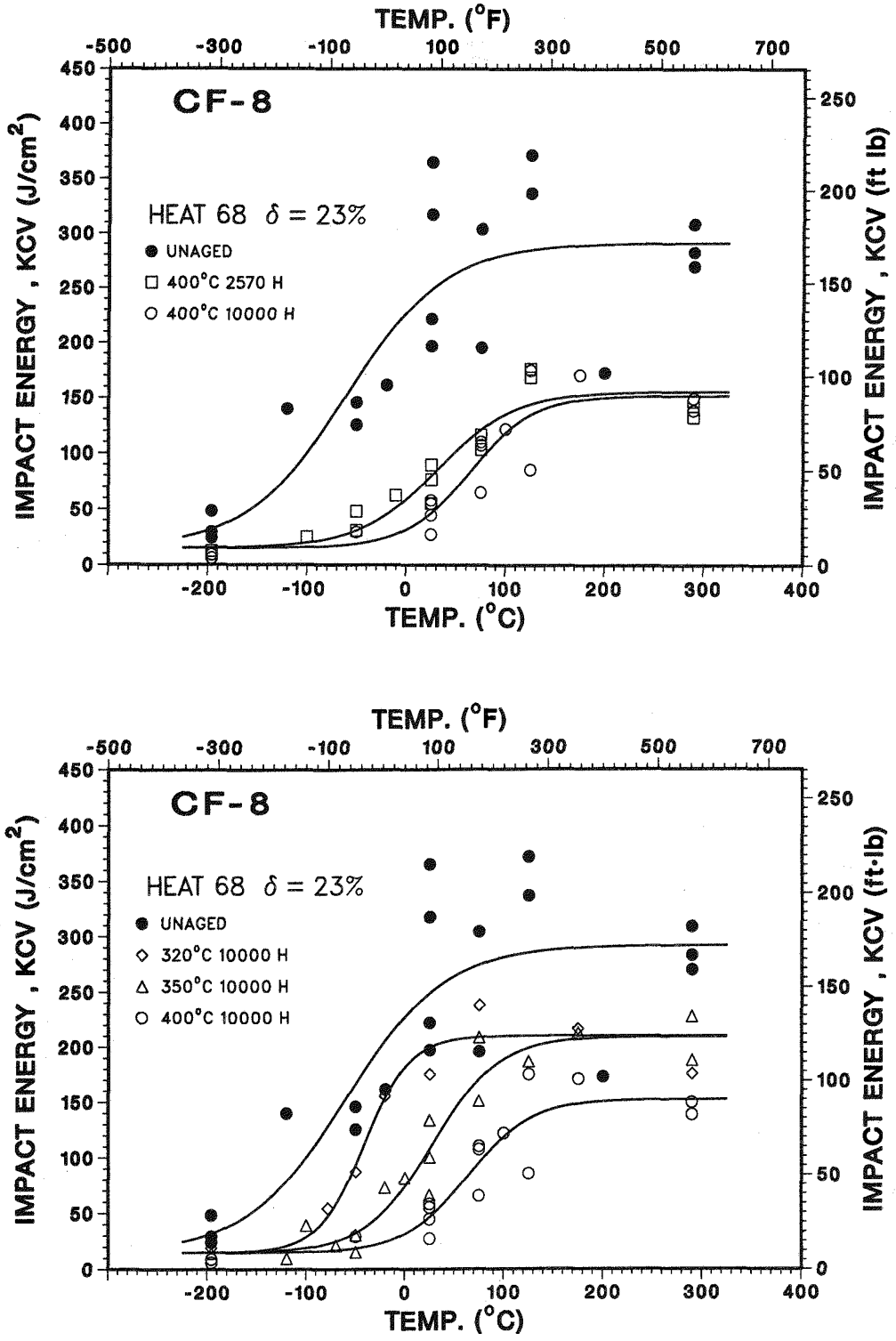

Fig. 21. Effect of Aging Time and Temperature on the Room Temperature Impact Energy of CF–8 Cast Stainless Steel.

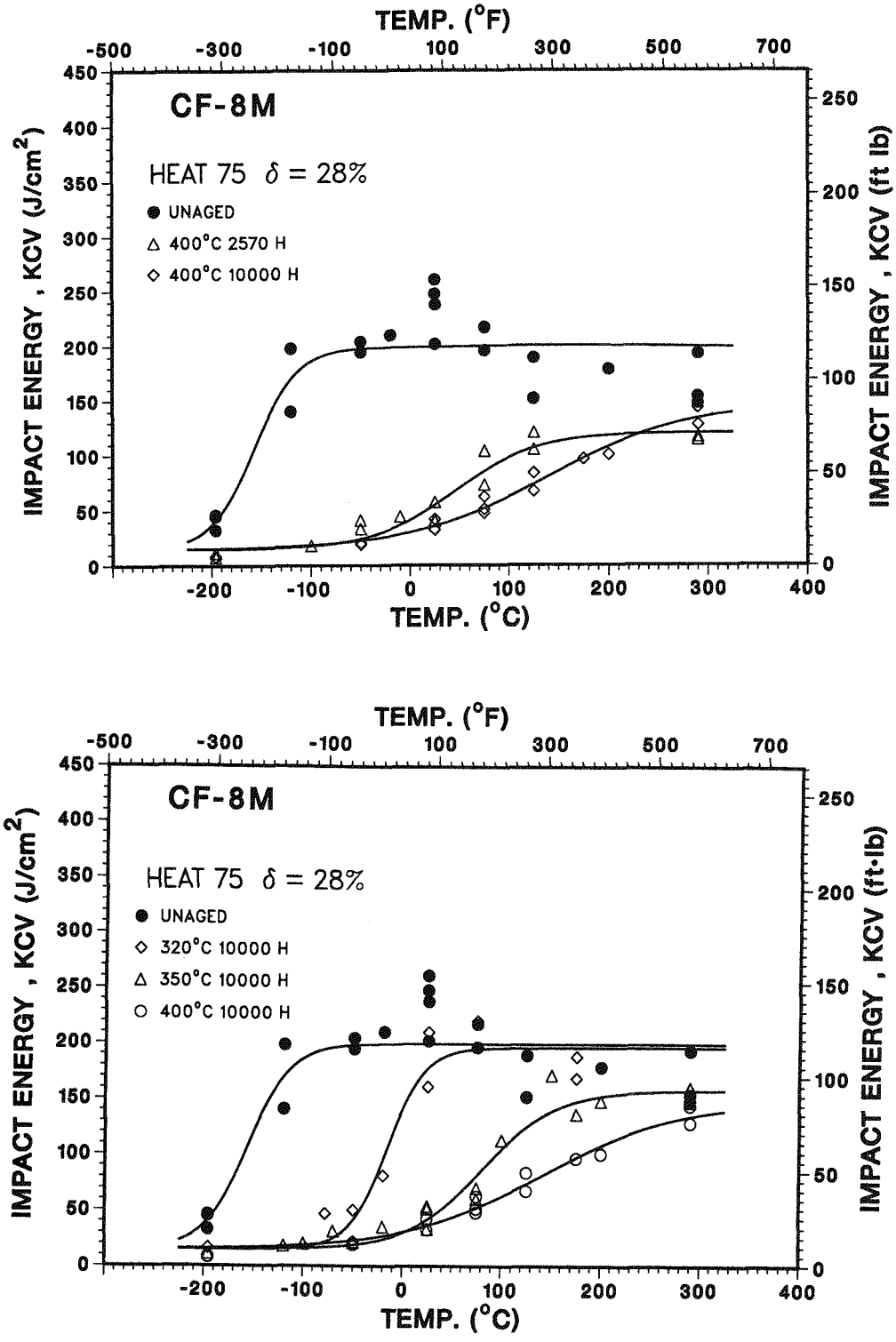

Fig. 22. Effect of Aging Time and Temperature on the Room Temperature Impact Energy of CF-8M Cast Stainless Steel.

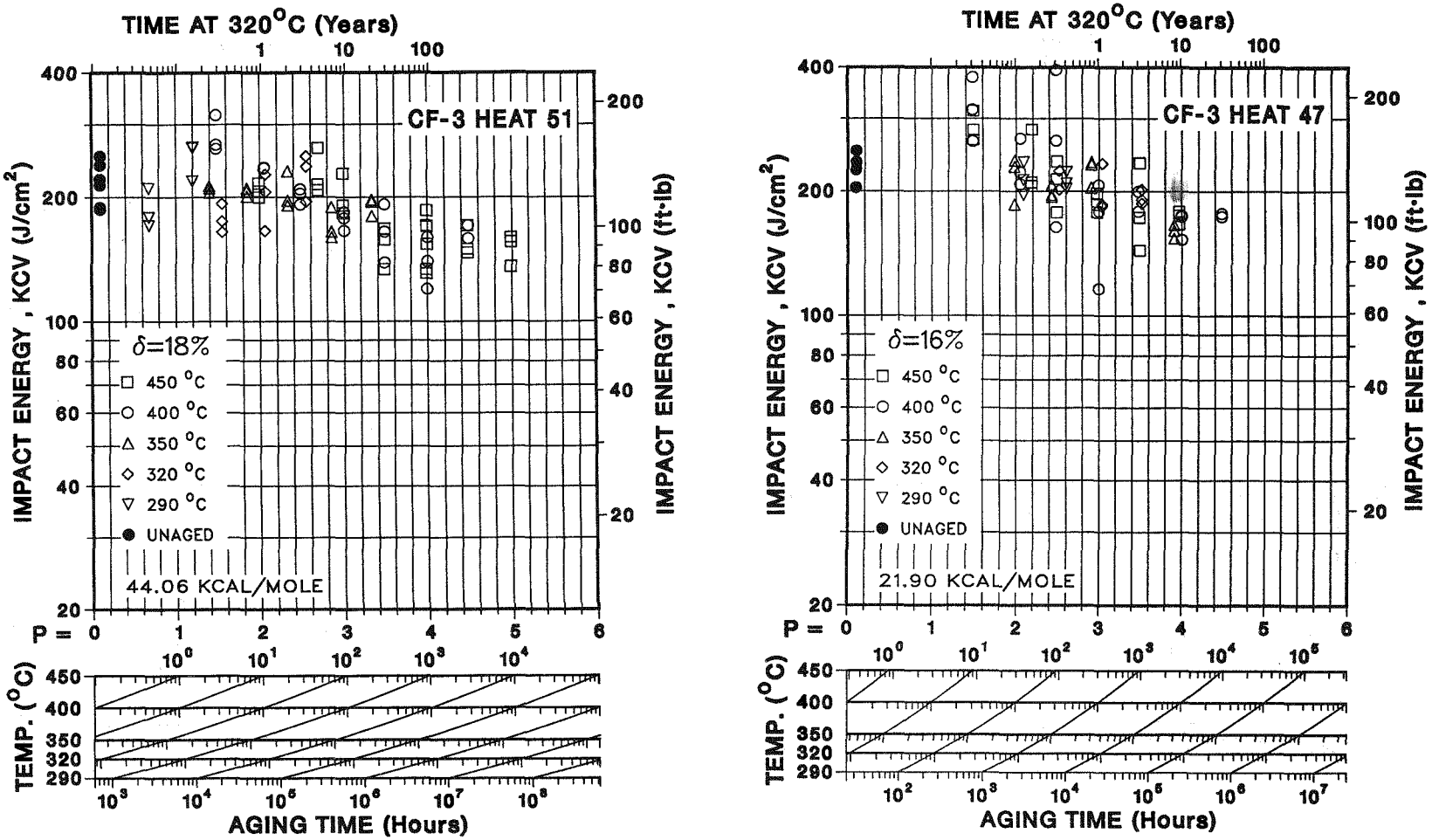

Fig. 23. Influence of Thermal Aging on the Room Temperature Impact Energy of CF-3 Cast Stainless Steel.

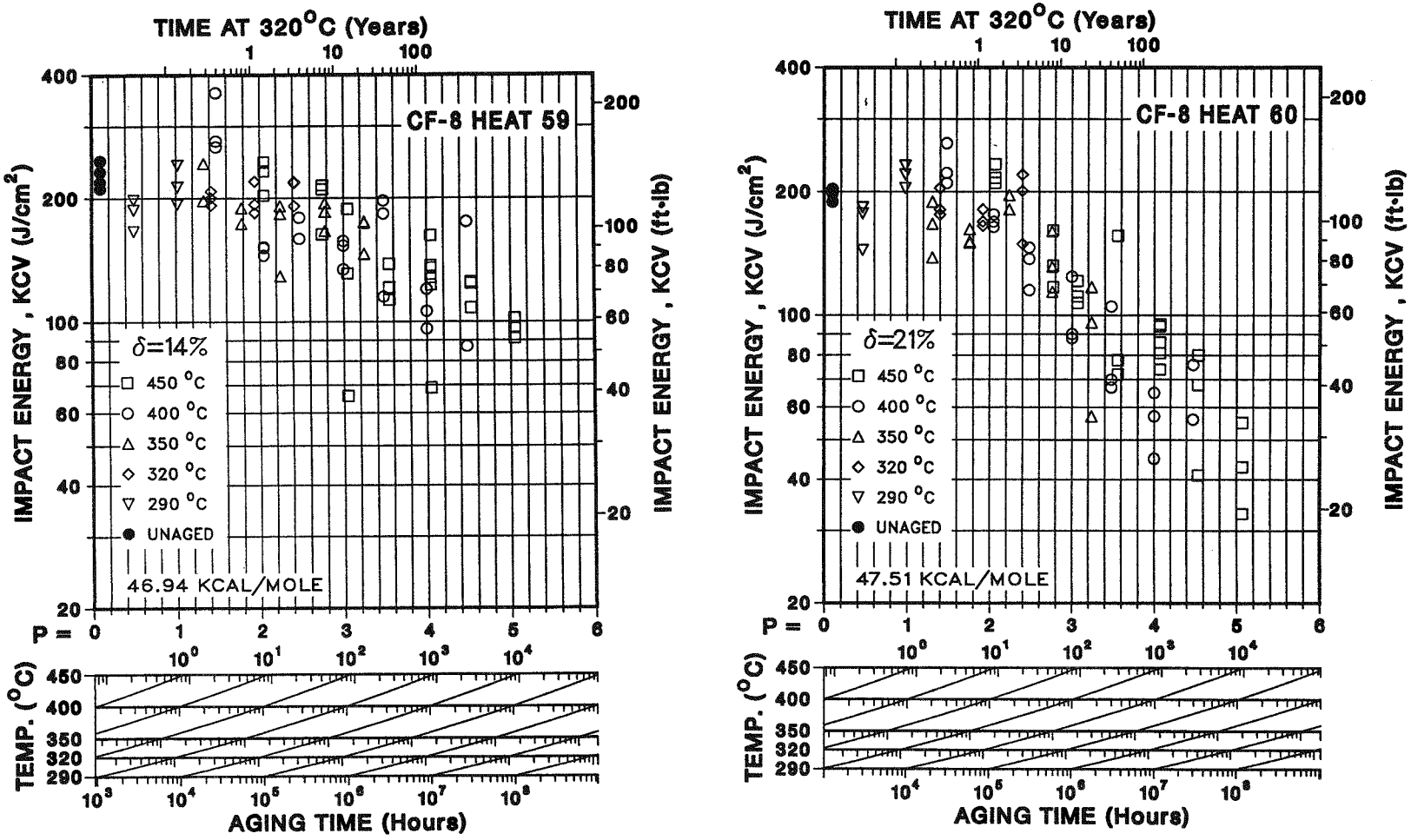

Fig. 24. Influence of Thermal Aging on the Room Temperature Impact Energy of CF-8 Cast Stainless Steel.

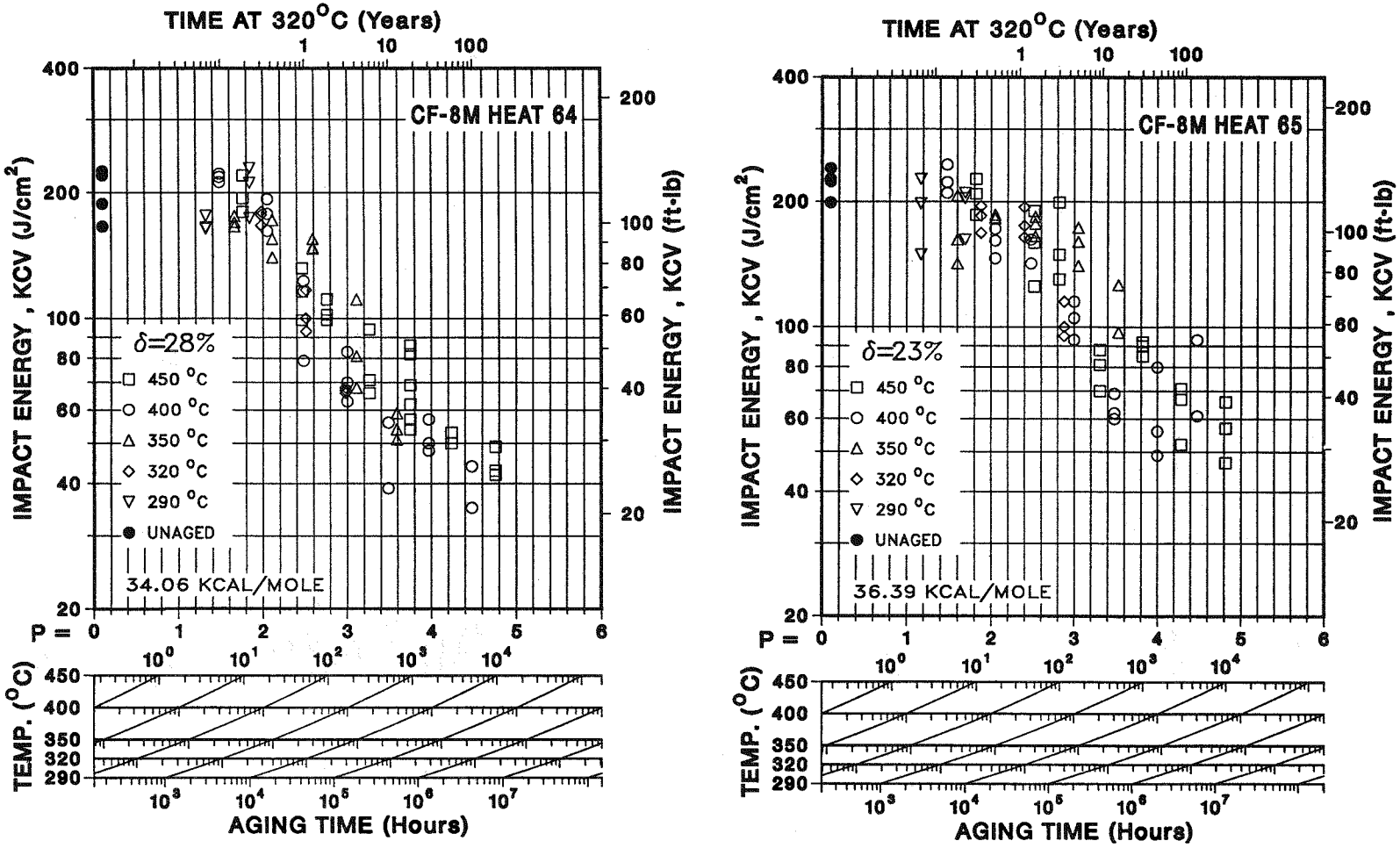

Fig. 25. Influence of Thermal Aging on the Room Temperature Impact Energy of CF-8M Cast Stainless Steel.

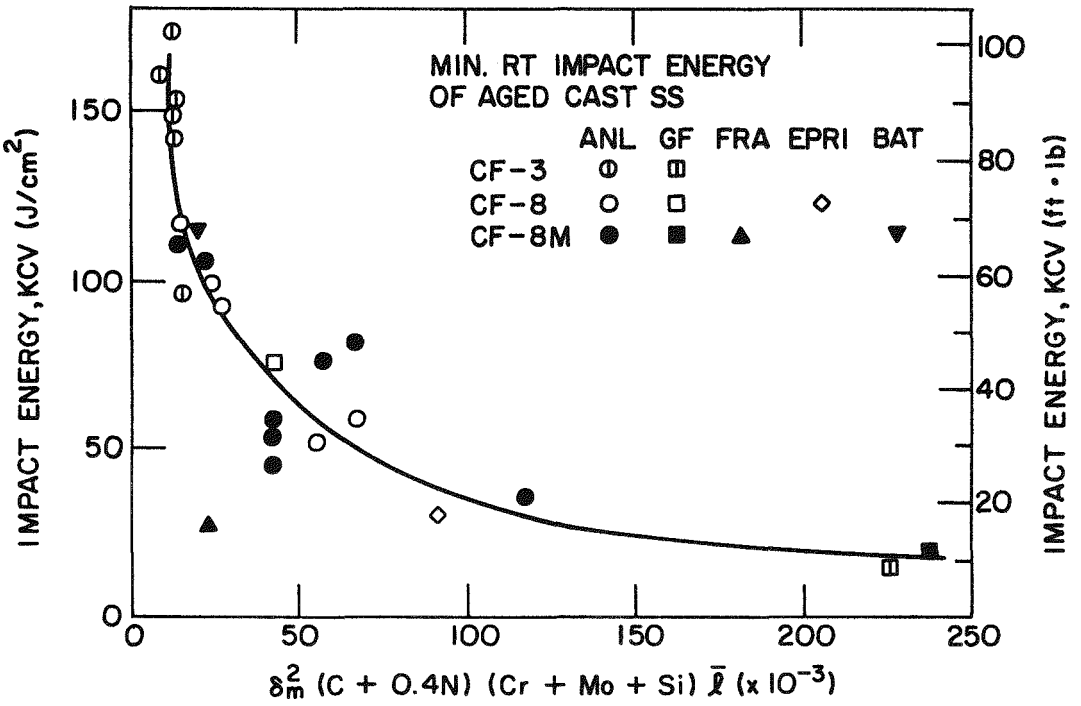

Fig. 26. Correlation between Minimum Room Temperature Impact Energy and Material Parameter for Aged Cast Stainless Steel.

indicate initiation of cleavage of the ferrite by carbide cracking. The present correlation does not consider the effects of Nb on embrittlement; it is not applicable to Nb-containing cast stainless steels.

The results indicate that the impact energy will be less than 50 J/cm^2 (~30 ft·lb) for those cast stainless steels for which the material parameter is greater than ~60. For cast stainless steels containing >10% ferrite, the mean ferrite spacing is in the range of 40 to 200 μm; Cr + Mo + Si concentration is ~22% for CF-8 or CF-3, and ~24% for CF-8M; and N content is typically 0.04%. Thus, for cast materials with 0.06% C and 100-μm ferrite spacing, the impact energy will be below 50 J/cm^2 when the ferrite content is above 20%. Cast materials with 10 or 15% ferrite can also reach very low impact strength when the ferrite spacing or the N content is high.

For all in-service cast stainless steels, the variables in the material parameter are readily available. The composition is known, ferrite content can be calculated from the composition or measured with a ferrite scope, and the ferrite spacing can be determined by a surface replica technique. Thus, Fig. 26 can be used to estimate the extent of embrittlement, i.e., the lowest room temperature impact energy that would ever be achieved for any given cast stainless steel component.

3.2.3 Kinetics of Embrittlement

The results from the present study and data from FRA[7,31] and GF[4] studies were analyzed to develop a correlation between the activation energy for embrittlement and

the chemical composition of the cast material. Initially, all major elements and C and N were included in the correlation. Elements with poor coefficients of correlation were then excluded. The analyses yielded two separate correlations: one for the ANL and FRA data, given by

$$Q(\text{kJ/mole}) = 90.54 + 9.62\,Cr - 8.12\,Ni - 7.53\,Mo + 20.59\,Si - 123.0\,Mn + 317.7\,N$$

or

$$Q(\text{kcal/mole}) = 21.64 + 2.30\,Cr - 1.94\,Ni - 1.8\,Mo + 4.92\,Si - 29.40\,Mn + 75.93\,N; \quad (4)$$

and the other for the GF data, given by

$$Q(\text{kJ/mole}) = -66.65 + 6.90\,Cr - 5.44\,Ni + 8.08\,Mo + 17.15\,Si + 44.1\,Mn + 297.1\,N$$

or

$$Q(\text{kcal/mole}) = -15.93 + 1.65\,Cr - 1.30\,Ni + 1.93\,Mo + 4.10\,Si + 10.54\,Mn + 71.00\,N. \quad (5)$$

The observed and predicted activation energies for the two data sets are plotted in Fig. 27. The coefficients for chromium, nickel, silicon, and nitrogen show the same behavior in the two correlations, however, the constants and the coefficients for molybdenum and manganese have opposite sign.

Equation (4) represents a wide range of material composition and was used to predict the activation energy of embrittlement of two heats of cast material not used in obtaining the correlation. The impact energies of the heats are plotted as a function of the aging parameter in Fig. 28. The data obtained for different aging temperatures follow a single curve. The results indicate that for both heats, the minimum values of impact energy will be reached within the reactor lifetime of 40 yr.

The reasons for separate expressions for the two data sets and different effects of constituent elements in the two expressions are not clearly understood. The precipitation or growth of phase boundary carbides or nitrides during aging would increase the activation energy of embrittlement. An increase in C or N in the steel will promote carbide or nitride precipitation and, thus, increase the activation energy. The positive sign of the coefficient for N agrees with this behavior; the C content in the steel gave a poor correlation.

The contribution of other elements, viz., Ni, Si, Mo, and Mn, is due to their effect on G-phase precipitation. These elements should promote G-phase precipitation; hence, the coefficients for these elements should have a negative sign, since G-phase precipitation decreases the activation energy of embrittlement. The coefficient for Si

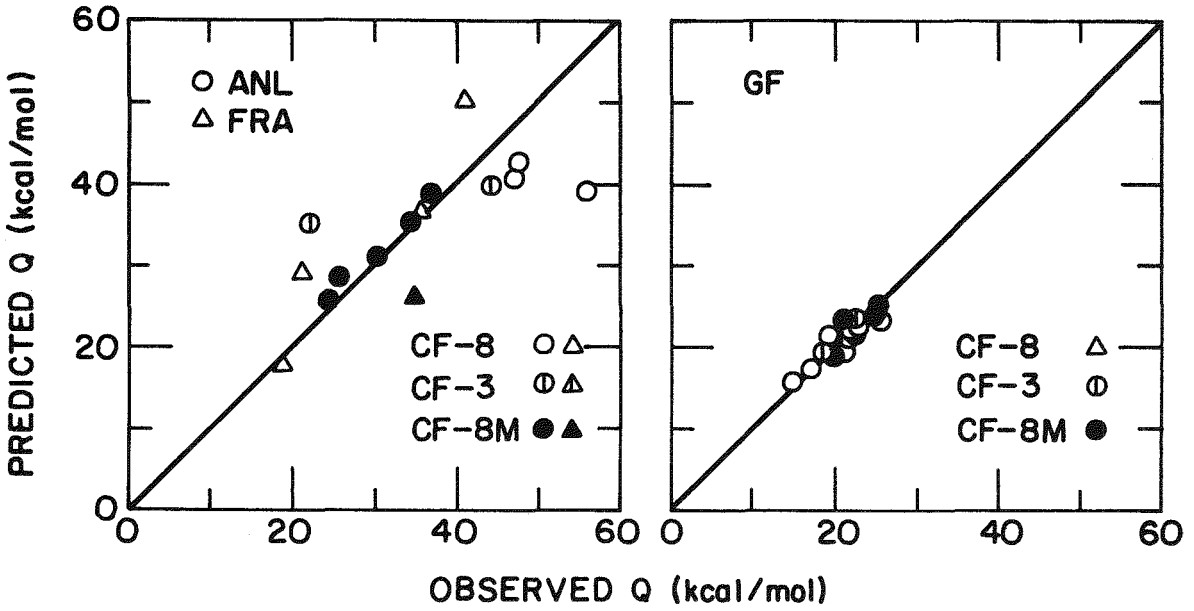

Fig. 27. Observed and Predicted Activation Energy for Low-Temperature Embrittlement of Cast Stainless Steel.

has a positive sign in both expressions, and coefficients for Mo and Mn are positive in Eq. (5). These results indicate that some other factors, not included in the analysis, influence the kinetics of embrittlement. The kinetics data are being analyzed to include these effects and to obtain a single expression for predicting the activation energy of embrittlement of cast stainless steels.

3.2.4 Recovery Anneal

Tests were conducted to investigate the possibility of recovering the loss of toughness of low-temperature-aged cast stainless steel. Studies on ferritic and martensitic steels have shown that the loss of toughness can be recovered by a short-term anneal at 550°C (1022°F). The time-temperature transformation curves for Fe-Cr alloys indicate that the α' phase is not stable at 550°C. However, these alloys are embrittled after aging for >10 h at 550°C owing to the formation of the sigma phase. Consequently, the embrittled cast materials were annealed for 1 h at 550°C to dissolve the α' and yet avoid the formation of sigma phase. The toughness of low-temperature embrittled cast stainless steel was virtually recovered by annealing at 550°C for 1 h and water quenching.[8,9] The dissolution of α' was confirmed by microstructural studies.[18]

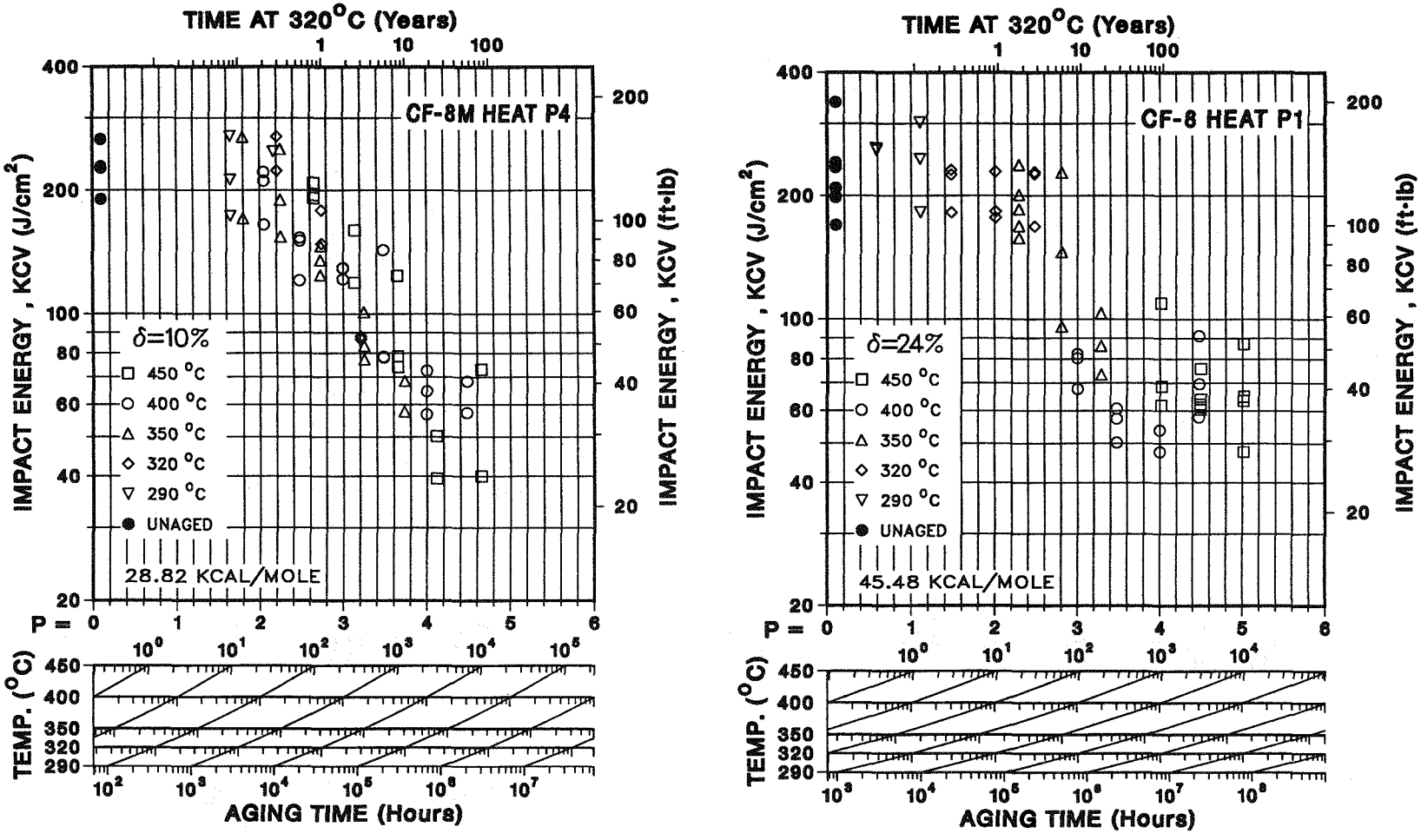

Fig. 28. Impact Energy vs Aging Parameter Curves Based on Calculated Activation Energy for CF-8M and CF-8 Cast Stainless Steel.

The ductile-to-brittle transition curves for the KRB pump cover plate material, after reactor service and reannealing for ~1 h at 550°C and water quenching, are shown in Fig. 29. The data for archive material from the KRB reactor pump cover plate are also included in the figure.* The results show an essentially complete recovery of toughness; the transition curve for the reannealed material agrees with the data for the archive material. The USE of the material increases from 247 to 330 J/cm^2 after reannealing and the mid-shelf transition temperature decreases from 37 to -16°C. Microstructural characterization of the reannealed material showed no α'; however, the size and distribution of the carbides and G phase were essentially the same as in the reactor-aged material.[18] These results indicate that formation of α' phase is the primary mechanism for strengthening of the ferrite in cast duplex stainless steels.

The anneal recovered material was aged up to 10,000 h at 320, 350, and 400°C to investigate its reembrittling behavior. The results are shown in Fig. 30. The material reembrittles in a relatively short time. For example, aging for 100 h at 400°C or 3,000 h at 320°C decreased the impact energy to the value observed after reactor service. After 3,000 h of aging at 400°C, the impact energy decreased to ~20 J/cm^2, a value close to the lower-shelf energy for the material.

It is not clear at present whether this behavior is typical of all reannealed cast stainless steels or is unique to this material. The metallurgical information for the KRB material, Table 1, yields a material parameter of ~200. Figure 26 indicates that the minimum room temperature impact energy for the KRB material is ~20 J/cm^2, the value obtained for the reannealed and aged specimens. A service time of ~8 yr at 284°C was insufficient to achieve the minimum impact energy. Recovery annealed material from other heats and grades of cast stainless steel are being aged to better establish the reembrittlement behavior.

3.2.5 Conclusions

Charpy-impact data for thermally aged cast stainless steel are analyzed to determine the kinetics and extent of embrittlement. The results show that the material composition and the ferrite content and spacing are important parameters in controlling embrittlement of cast stainless steels. The ferrite morphology has a strong effect on the extent of embrittlement, whereas the material composition influences the kinetics of embrittlement. The results indicate that the kinetics of embrittlement can vary significantly with the composition of the cast material; the activation energy of embrittlement varies between 90 and 235 kJ/mole (20 and 56 kcal/mole).

Mechanical-property results from the present study and data from other investigations were analyzed to develop the procedure and correlations for predicting the kinetics and extent of embrittlement, under reactor operating conditions, from the material parameters. Correlations for predicting the toughness loss at reactor temperatures are being developed. Mechanical tests are in progress on long-term laboratory-aged material and reactor-aged material to validate and/or modify the correlations.

---

*A. Trautwein, Georg Fischer Co., private communication, February 1986.

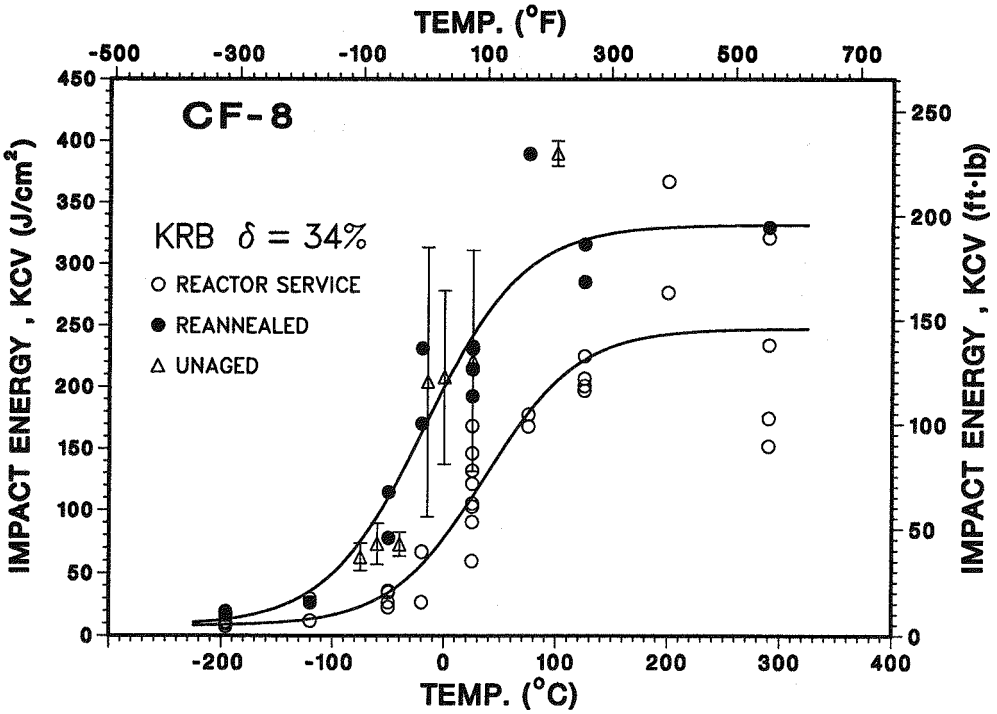

Fig. 29. Effect of Reannealing on the Ductile-to-Brittle Transition Curve for the KRB Pump Cover Plate Material.

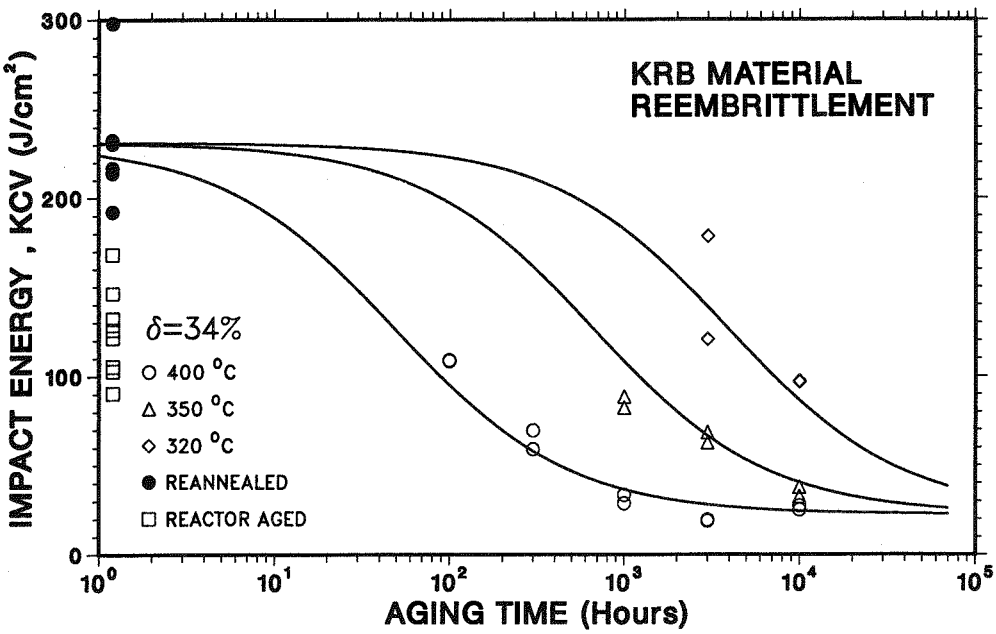

Fig. 30. Reembrittlement Behavior of Recovery Annealed KRB Pump Cover Plate Material.

The toughness of cast stainless steels during embrittlement can be recovered by a short-term anneal of 1 h at 550°C and water quenching. However, preliminary data show that the anneal-recovered material reembrittles in a relatively short time. Tests are being conducted on cast materials of different grades to better understand the recovery anneal and reembrittlement behavior of cast stainless steels.

References

1. J. J. Heger, "885°F Embrittlement of the Ferritic Chromium-iron Alloys," *Metal Prog.* August 1951, pp. 55–61.

2. P. J. Grobner, "The 885°F (475°C) Embrittlement of Ferritic Stainless Steels," *Metall. Trans.* **4**, 251–260 (1973).

3. T. J. Nichol, A. Datta, and G. Aggen, "Embrittlement of Ferritic Stainless Steels," *Metall. Trans.* **11A**, 573 (1980).

4. A. Trautwein and W. Gysel, "Influence of Long Time Aging of CF-8 and CF-8M Cast Steel at Temperatures between 300 and 500°C on the Impact Toughness and the Structure Properties," *Spectrum, Technische Mitteilungen aus dem+GF+Konzern*, No. 5 (May 1981); in *Stainless Steel Castings*, V. G. Behal and A. S. Melilli, eds., ASTM STP 756, Philadelphia, 1982, pp. 165–189.

5. G. Baudry and C. Pichard, "Evolution during Long Holding Times at 300 and 450°C of the Mechanical Properties of Austeno-Ferritic Steel Castings and Welded Joints Used in Pressurized Water Nuclear Reactors," in *Troisieme Congres National sur la Technologie des Appareils a Bression*, Vol. 2, Materiaux, A.F.I.A.P., 1980, p. 673.

6. E. I. Landerman and W. H. Bamford, "Fracture Toughness and Fatigue Characteristics of Centrifugally Cast Type 316 Stainless Steel Pipe after Simulated Thermal Service Conditions," in *Ductility, and Toughness Considerations in Elevated Temperature Service*, ASME MPC-8, New York, 1978, pp. 99-125.

7. G. Slama, P. Petrequin, and T. Magep, "Effect of Aging on Mechanical Properties of Austenitic Stainless Steel Castings and Welds," presented at SMIRT Post-Conference Seminar 6, *Assuring Structural Integrity of Steel Reactor Pressure Boundary Components*, August 29-30, 1983, Monterey, CA.

8. O. K. Chopra and H. M. Chung, "Aging Degradation of Cast Stainless Steels: Effects on Mechanical Properties," in *Environmental Degradation of Materials in Nuclear Power Systems–Water Reactors*, Proc. Third Int. Symp., Traverse City, MI, August 30–September 3, 1987, G. J. Theus and J. R. Weeks, eds., The Metall. Soc., Warrendale, PA 1988, pp. 737-748.

9. O. K. Chopra and H. M. Chung, "Effect of Low-Temperature Aging on the Mechanical Properties of Cast Stainless Steels," in *Properties of Stainless Steels in Elevated Temperature Service*, M. Prager, ed., MPC-Vol. 26, PVP-Vol. 132, ASME, New York, 1988, pp. 79–105.

10. O. K. Chopra and H. M. Chung, "Long-Term Embrittlement of Cast Duplex Stainless Steels in LWR Systems: Annual Report," October 1983-September 1984, NUREG/CR-4204, ANL-85-20 (March 1985); *Nucl. Eng. Des.* **89**, 305 (1985).

11. O. K. Chopra and H. M. Chung, "Long-Term Embrittlement of Cast Duplex Stainless Steels in LWR Systems: Annual Report," October 1984-September 1985, NUREG/CR-4503, ANL-86-3 (January 1986).

12. O. K. Chopra and H. M. Chung, "Long-Term Embrittlement of Cast Duplex Stainless Steels in LWR Systems: Semiannual Report," October 1985-March 1986, NUREG/CR-4744 Vol. I, No. 1, ANL-86-54 (September 1986).

13. O. K. Chopra and G. Ayrault, "Long-Term Embrittlement of Cast Duplex Stainless Steels in LWR Systems," in *Materials Science and Technology Division Light-Water-Reactor Safety Research Program: Quarterly Progress Report*, October-December 1983, NUREG/CR-3689 Vol. IV, ANL-83-85 Vol. IV, pp. 129-151 (August 1984).

14. O. K. Chopra and H. M. Chung, "Long-Term Embrittlement of Cast Duplex Stainless Steels in LWR Systems," in *Materials Science and Technology Division Light-Water-Reactor Safety Materials Engineering Research Programs: Quarterly Progress Report*, January-March 1984, NUREG/CR-3998 Vol. I, ANL-84-60 Vol. I, p. 52 (September 1984).

15. O. K. Chopra and H. M. Chung, "Long-Term Embrittlement of Cast Duplex Stainless Steels in LWR Systems: Semiannual Report," October 1986–March 1987, NUREG/CR-4744 Vol. 2, No. 1, ANL-87-45 (July 1987).

16. O. K. Chopra and H. M. Chung, "Long-Term Embrittlement of Cast Duplex Stainless Steels in LWR Systems: Semiannual Report," April–September 1987, NUREG/CR-4744 Vol. 2, No. 2, ANL-89/6 (August 1989).

17. H. M. Chung and O. K. Chopra, "Microstructure of Cast Duplex Stainless Steel after Long-Term Aging," in *Proc. Second Int. Symp. on Environmental Degradation of Materials in Nuclear Power Systems - Water Reactors*, Am. Nucl. Soc., LaGrange Park, IL, 1986, pp. 287-292.

18. H. M. Chung and O. K. Chopra, "Kinetics and Mechanism of Thermal Aging Embrittlement of Duplex Stainless Steels," in *Environmental Degradation of Materials in Nuclear Power Systems–Water Reactors*, G. J. Theus and J. R. Weeks, eds., The Metall. Soc., 1988, Warrendale, PA, pp. 359–370.

19. H. M. Chung and O. K. Chopra, "Long-Term Aging Embrittlement of Cast Austenitic Stainless Steels - Mechanism and Kinetics," in *Properties of Stainless Steels in Elevated Temperature Service*, M. Prager, ed., MPC–Vol. 26, PVP–Vol. 132, ASME, New York, 1988, pp. 17-34.

20. W. J. Shack, O. K. Chopra, and H. M. Chung, "Shippingport Aging Studies–Results and Plans," *Proc. 16th Water Reactor Safety Information Meeting*, Gaithersburg, MD, October 24–27, 1988, NUREG/CP–0097, Vol. 3, March 1989, pp. 547–562.

21. H. M. Chung and O. K. Chopra, "Characterization of Duplex Stainless Steels by TEM, SANS, and APFIM Techniques," in *Proc. Int. Metallographic Symp. Characterization of Advanced Materials*, Monterey, CA, July 27–29, 1987.

22. H. D. Solomon, "Investigation of the Physical Metallurgy, Mechanical Properties, and Embrittlement of Alloy U50," General Electric Co. Report 76CRD 188 (April 1977).

23. K. N. Akhurst and P. H. Pumphrey, "The Aging Kinetics of CF–3 Cast Stainless Steel in the Temperature Range 300°C to 400°C," RO/L/3354/R88, Central Electricity Generating Board Research Laboratories, Leatherhead, United Kingdom (November 1988).

24. H. D. Solomon and L. M. Levinson, "Mössbauer Effect Study of '475°C Embrittlement' of Duplex and Ferritic Stainless Steels," *Acta Met.* **26**, 429–442 (1978).

25. H. M. Chung, "Thermal Aging of Some Decommissioned Reactor Cast Stainless Steel Components and Methodology for Life Prediction," paper submitted to ASME–Material Properties Council Symp. on Plant Life Extension for Nuclear Components, July 24–27, 1989, Honolulu.

26. W. H. Bamford, F. J. Witt, and S. A. Swamy, "Aging Effects on Cast Stainless Steels," in *Properties of Stainless Steels in Elevated Temperature Service*, ed. M. Prager, MPC–Vol. 26, PVP–Vol. 132, ASME, New York, 1987, pp. 49–63.

27. M. K. Miller and J. Bentley, "Characterization of Fine-Scale Microstructures in Aged Primary Coolant Pipe Steels," in *Proc. 3rd Int. Symp. on Environmental Degradation of Materials in Nuclear Power Systems–Water Reactors*, August 30–September 3, 1987, Traverse City, MI, G. J. Theus and J. R. Weeks, eds., The Metall. Soc., Warrendale, PA, 1988, pp. 341–349.

28. F. A. Garner, H. R. Brager, and J. N. McCarthy, "Neutron–induced Spinodal–like Decomposition of Fe–Ni and Fe–Ni–Cr Alloys," in *Radiation–Induced Changes in Microstructure: 13th Intl. Symp.* (Part I), ASTM STP 955, F. A. Garner, N. H. Packan, and A. S. Kumar, eds., ASTM., Philadelphia, 1987, pp. 775–787.

29. J. Danon, R. B. Scorzelli, I. Souza Azevedo, W. Curvello, J. F. Albertsen, and J. N. Knudsen, "Iron–Nickel 50–50 Superstructure in the Santa Catharina Meteorite," *Nature* **277**,,284 (1979).

30. R. B. Scorzelli and J. Danon, "Mössbauer Spectroscopy and X–Ray Diffraction Studies of Fe–Ni Order–Disorder Processes in a 35% Ni Meteorite (Santa Catharina)," *Phy. Scripta* **32**, 143 (1985).

31. Y. Meyzaud, P. Ould, P. Balladon, M. Bethmont, and P. Soulat, "Tearing Resistance of Aged Cast Austenitic Stainless Steel," paper presented at *Int. Conf. on Thermal Reactor Safety* (NUCSAFE 88), October 1988, Avignon, France.

Distribution for NUREG/CR-4744 Vol. 3, No. 1 (ANL-89/22)

Internal:

O. K. Chopra (15)
H. M. Chung (15)
C. Malefyt
W. J. Shack
C. E. Till
R. W. Weeks
TIS Files (3)
ANL Patent File
ANL Contract File
ANL Libraries (2)

External:

NRC, for distribution per R5 (315)
Manager, Chicago Operations Office, DOE
Materials and Components Technology Division Review Committee
P. Alexander, Lord Corporation, Erie, PA
M. S. Dresselhaus, Massachusetts Institute of Technology, Cambridge, MA
S. J. Green, Electric Power Research Institute, Palo Alto, CA
R. A. Greenkorn, Purdue U., West Lafayette, IN
L. J. Jardine, Lawrence Livermore National Laboratory
C. Y. Li, Cornell U., Ithaca, NY
R. E. Scholl, Counter Quake Corp., Redwood City, CA
P. G. Shewmon, Ohio State U., Columbus, OH
R. E. Smith, Electric Power Research Institute, N.D.E. Ctr., Charlotte, NC
C. B. Alcock, U. Toronto
D. Atteridge, Battelle Pacific Northwest Lab., P. O. Box 999, Richland, WA 99352
W. H. Bamford, Westinghouse Electric Corp., WNES, Box 355, Pittsburgh, PA 15230
N. G. Cofie, Nutech, 145 Martinvale Lane, San Jose, CA 95119
A. Cowan, Risley Nuclear Power Development Labs., UKAEA (Northern Div.), Risley, Warrington WA3 6AT, United Kingdom
E. L. Creamer, Shell Oil Co., Box 3105, Houston, TX 77253-3105
W. H. Cullen, Materials Engineering Associates, Inc., 9700 B. George Palmer Highway, Lanham, MD 20706
B. J. L. Darlaston, CEGB, Berkeley Nuclear Laboratories, Berkeley, Gloucestershire GL13 9PB, United Kingdom
H. Domian, Alliance Research Center, Babcock & Wilcox Co., Alliance, OH 44601
M. Guttmann, Electricite de France, Les Renardieres Roule de Sens, 77 Ecuelles, France
W. Gysel, Georg Fischer, Ltd., Schaffhausen, Switzerland
P. Hedgecock, APTECH Engineering Services, Inc., 795 San Antonio Road, Palo Alto, CA 94303
B. Hemsworth, HM Nuclear Installations Inspectorate, Thames House North, Millbank, London, SW1P 42J, United Kingdom
C. G. Interrante, Center for Materials Science, National Bureau of Standards, Gaithersburg, MD 20899
J. Jansky, Buro fur Technische Beratung, Rilkestrabe 5, 7250 Leonberg, West Germany
C. E. Jaske, Battelle Columbus Laboratories, 505 King Ave., Columbus, OH 43201-2693
D. de G. Jones, Matls. Sci. Div., Atomic Energy Corp., Private Bag X256, Pretoria 0001, South Africa
C. Kim, Westinghouse Electric Corp., GTS Div., Box 2728, Pittsburgh, PA 15230-2728

P. M. Lang, Office of Converter Reactor Deployment, USDOE, Washington, DC
G. J. Licina, Structural Integrity Associates, 3150 Almaden Exp., Suite 226, San Jose, CA 95118
T. R. Mager, Westinghouse Electric Corp., GTS Div., Box 2728, Pittsburgh, PA 15230-2728
Y. Meyzaud, Framatome, Tour FIAT, Cedex 16, 92084, Paris, France
D. M. Norris, Electric Power Research Inst., P. O. Box 10412, Palo Alto, CA 94303
M. Prager, Materials Properties Council, Inc., 345 East 47th Street, New York, NY 10017
P. H. Pumphrey, Central Electricity Generating Board, Research Lab., Leatherhead, Surrey, England
V. K. Sikka, Oak Ridge National Lab., P. O. Box 2008, Oak Ridge, TN 37831
G. Slama, Framatome, Tour FIAT, Cedex 16, 92084 Paris La Defense, France
G. D. W. Smith, Oxford University, Dept. of Metallurgy and Material Science, Oxford, England
H. D. Solomon, General Electric Co., P. O. Box 43, Schenectady, NY 12301
D. M. Stevens, Lynchburg Research Center, Babcock & Wilcox Co., P. O. Box 239 Lynchburg, VA 24505
L. Taylor, National Nuclear Corp., Cambridge Rd., Whetstone, Leicester LE8 3LH, England
R. A. Walker, The Welding Institute, Abington Hall, Abington, Cambridge, CB1 6AL, England
J. Wilks, AMOCO, Whiting Refinery, Whiting, IN 46394

NRC FORM 335 (2-89) NRCM 1102, 3201, 3202

U.S. NUCLEAR REGULATORY COMMISSION

BIBLIOGRAPHIC DATA SHEET

(See instructions on the reverse)

1. REPORT NUMBER (Assigned by NRC. Add Vol., Supp., Rev., and Addendum Numbers, if any.)

NUREG/CR-4744
Vol. 3, No. 1
ANL-89/22

2. TITLE AND SUBTITLE

Long-Term Embrittlement of Cast Duplex Stainless Steels In LWR Systems

Semiannual Report
October 1987-March 1988

3. DATE REPORT PUBLISHED

MONTH	YEAR
February	1990

4. FIN OR GRANT NUMBER

A2243

5. AUTHOR(S)

O. K. Chopra, H. M. Chung

6. TYPE OF REPORT

Technical; Semiannual

7. PERIOD COVERED *(Inclusive Dates)*

8. PERFORMING ORGANIZATION – NAME AND ADDRESS *(If NRC, provide Division, Office or Region, U.S. Nuclear Regulatory Commission, and mailing address; if contractor, provide name and mailing address.)*

Argonne National Laboratory
9700 South Cass Avenue
Argonne, IL 60439

9. SPONSORING ORGANIZATION – NAME AND ADDRESS *(If NRC, type "Same as above"; if contractor, provide NRC Division, Office or Region, U.S. Nuclear Regulatory Commission, and mailing address.)*

Division of Engineering
Office of Nuclear Regulatory Research
U.S. Nuclear Regulatory Commission
Washington, DC 20555

10. SUPPLEMENTARY NOTES

11. ABSTRACT *(200 words or less)*

This progress report summarizes work performed by Argonne National Laboratory on long-term embrittlement of cast duplex stainless steels in LWR systems during the six months from October 1987 to March 1988. A mechanistic understanding of the activation energy of aging is described on the basis of the results of microstructural characterization of various heats of Grades CF–3, CF–8, and CF–8M stainless steel that were used in aging studies at different laboratories. The kinetics of the spinodal decomposition of ferrite (i.e., the primary mechanism of aging embrittlement) appear to be strongly influenced by a synergistic effect of G–phase nucleation and growth. When the activation energies (ranging from 18 to 50 kcal/mole) were plotted as a function of the volume fraction of G phase produced during accelerated aging, a good correlation was obtained regardless of variations in grade, bulk chemical composition, and fabrication process. Spinodal–like decomposition of austenite in heats containing a relatively high level of Ni has also been investigated. Charpy-impact data for thermally aged cast stainless steel were analyzed to determine the kinetics and extent of embrittlement. The ferrite morphology had a strong effect on the extent of embrittlement, whereas the material composition influenced the kinetics of embrittlement. Results obtained from the present study of mechanical properties, and data of other investigators were analyzed to develop the procedure and correlations for predicting the kinetics and extent of embrittlement, under reactor operating conditions, from the material parameters.

12. KEY WORDS/DESCRIPTORS *(List words or phrases that will assist researchers in locating the report.)*

Cast Stainless Steel
Aging
Precipitation
Spinodal Decomposition
Fracture Toughness
Impact Energy
Tensile Strength
Activation Energy

13. AVAILABILITY STATEMENT

Unlimited

14. SECURITY CLASSIFICATION

(This Page) Unclassified

(This Report) Unclassified

15. NUMBER OF PAGES

16. PRICE